

Production of EMRIs in Supermassive Black Hole Binaries

J. Nate Bode^{1,2*} and Christopher Wegg^{1,3†}

¹*Theoretical Astrophysics, California Institute of Technology, M/C 350-17, Pasadena, CA 91125.*

²*Boston Consulting Group, 300 N. LaSalle Ave, Chicago, Ill, 60654*

³*Max-Planck-Institut für Extraterrestrische Physik, Giessenbachstrasse, 85748 Garching, Germany.*

18 October 2018

ABSTRACT

We consider the formation of extreme mass-ratio inspirals (EMRIs) sourced from a stellar cusp centred on a primary supermassive black hole (SMBH) and perturbed by an inspiraling less massive secondary SMBH. The problem is approached numerically, assuming the stars are non-interacting over these short timescales and performing an ensemble of restricted three-body integrations. From these simulations we see that not only can EMRIs be produced during this process, but the dynamics are also quite rich. In particular, most of the EMRIs are produced through a process akin to the Kozai-Lidov mechanism, but with strong effects due to the non-Keplerian stellar potential, general relativity, and non-secular oscillations in the angular momentum on the orbital timescale of the binary SMBH system.

Key words: Black hole physics – gravitational waves – stars: kinematics and dynamics.

1 INTRODUCTION

One of the most interesting sources for low frequency gravitational wave (GW) detectors such as the final incarnation of the *Laser Interferometer Space Antenna* (LISA), or its newer scion European LISA (eLISA), is the capture of stellar mass compact objects (COs) by a supermassive black hole (SMBH). COs are the final state of stellar evolution and include stellar mass black holes, neutron stars, and white dwarfs. Due to the significant mass difference between the SMBH and the inspiraling CO, these sources are referred to as extreme mass-ratio inspirals (EMRIs).

Detection of EMRIs by GW detectors provides: 1) an accurate measurement of the spin and mass of the SMBH (Barack & Cutler 2004) along with a moderate determination of its location, 2) a test that the spin and mass are the only parameters characterizing the black hole’s space-time (termed ‘bothrodesy’; Ryan 1997; Hughes 2009), 3) information about the presence of a secondary SMBH orbiting the primary SMBH (Yunes, Miller & Thornburg 2011), 4) information about the presence of a gaseous disk in the system (Narayan 2000; Yunes et al. 2011), and 5) a possible electromagnetic counterpart to the LISA signal (Sesana et al. 2008; Menou, Haiman & Kocsis 2008) if the source was a white dwarf. Such an electromagnetic counterpart would localise the host, thus allowing for follow up observation.

The production of EMRIs amounts to either forming COs on, or driving them onto, orbits whose GW inspiral time is shorter than the timescale for other orbital perturbations. The standard method of EMRI production (Hills & Bender 1995) is that COs are transported to the EMRI loss cone via gravitational scattering with other

stellar mass objects. This is an improbable event because, as the CO’s orbit becomes more eccentric and the rate of orbital energy loss to GW emission increases, ever smaller kicks to its angular momentum may remove it from this orbit or plunge it directly into the central SMBH. Despite the apparent unlikelihood of this process, many such EMRIs are expected to form, and be observable by low frequency gravitational wave missions (see Amaro-Seoane et al. 2007, for a review of the subject).

Other possible EMRI formation mechanisms include the in situ formation of COs via a massive self-gravitating accretion disk (Levin 2003) like that which is believed to have existed in the Milky Way (Levin & Beloborodov 2003). Alternatively, the CO can be deposited close to the SMBH by a stellar binary which interacts strongly with the SMBH and ejects the CO’s partner, while leaving the CO on a low eccentricity orbit with small semi-major axis (Miller et al. 2005).

We consider a different scattering method; one where a secondary SMBH is present and entering the final stage of its inspiral (Begelman, Blandford & Rees 1980; Milosavljević & Merritt 2003) due to dynamical friction. In this scenario the scattering phase is short-lived, but the rate of stars scattered to highly eccentric orbits is significantly increased. Moreover, the secondary SMBH induces Lidov-Kozai oscillations in the orbital elements of many stars, considered first in the context of tidal disruptions by Ivanov, Polnarev & Saha (2005). Because some of these stars are COs, on passages close to the primary SMBH, they are not tidally disrupted, but instead radiate a fraction of their orbital energy in gravitational waves, leaving for the possibility of ultimately becoming an EMRI.

We investigate this possibility by performing an ensemble of three body integrations. The equations of motion of a star randomly chosen from a stellar cusp centred on a primary supermassive black hole (SMBH) are integrated in the presence of a secondary SMBH

* E-mail: natebode@gmail.com

† E-mail: wegg@mpe.mpg.de

inspiraling on a pre-calculated path determined by dynamical friction (Sec. 3.6). We consider a $10^6 M_\odot$ primary SMBH and various masses of the secondary SMBH and stars. The stars are then followed to determine if they eventually become EMRIs. For clarity we add that throughout the epochs of SMBH binary evolution we consider GW radiation has no practical effect on the SMBH orbit.

We present the results as follows. In Sec. 2 we present a brief introduction to EMRI formation under the standard channel, while we describe the assumptions and physical setup in Sec. 3. The simulation is described in Sec. 4 and the resulting rates are provided in Sec. 5. To understand the dynamics which result in the majority of our EMRIs we elucidate the standard Kozai-Lidov mechanism, as well as extensions, in Sec. 6. Our rates and the relevance of the assumptions they are based on are discussed in Sec. 7. In Sec. 8 we present our conclusions.

2 BACKGROUND

2.1 Parameter Space

Many of the key aspects of the standard method of EMRI formation are illustrated in Fig. 1 where we plot $a(1 - e)$ as a function of a , where a and e are the stars' semi-major axis and eccentricity, respectively. A star lying in this region of parameter space will inspiral due to GW radiation along curves like the solid red lines, and would take approximately the period of time labeled along the blue dashed lines to complete the inspiral, assuming no other interactions. Both are calculated using the approximate expressions in Peters (1964). A star lying below the solid grey line would likely turn into an EMRI, while one above would likely undergo some stellar scattering event which would increase its angular momentum (moving it upwards in the figure) and ultimately put it on a new trajectory with a much longer inspiral time. For reference and illustrative purposes we also plot the initial conditions of the 10^6 stars we simulate. These stars are also appropriate for the standard EMRI formation, since they are drawn from a stellar distribution (Eqn. 4) in the absence of the secondary. For these highly eccentric orbits, in the standard EMRI picture, weak stellar scatterings extract or add angular momentum from a star while keeping its energy approximately constant. This moves the star up or down in the figure. When the star scatters below the gray line, gravitational radiation can extract energy from the orbit faster than it is likely to be perturbed by star-star scatterings, thus leaving the star to inspiral along the red lines.

In the case presented in this paper, the picture is similar, but more intricate and rich. Kozai oscillations, along with significant apsidal precession due to the stellar potential and general relativity (GR), drive the stars on an orbital evolution which also conserves the orbital energy while causing the angular momentum to rise and fall before a close passage with the primary SMBH occurs. If the star passes close enough to the primary SMBH that a significant fraction of the star's orbital energy can be radiated in GWs, it can quickly circularise and form an EMRI. To elucidate these points the path of an EMRI formed in one of our simulations is shown in thin solid brown. The same star is also marked by a red-outlined gold star in Figs. 4, 6, and 7 and used to demonstrate the relative importance of the stellar potential and GR in Fig. 3. Like many of the EMRIs formed in our simulations this star begins with a low eccentricity orbit and with a semi-major axis about a factor of 10 smaller than the stalling radius of the secondary SMBH. It is only through an intricate interplay between the Kozai effect, precession

due to the stellar potential (SP precession) and GR effects that the star is driven to high eccentricity, has strong interactions with the primary SMBH and ultimately forms an EMRI.

2.2 Nomenclature and Notation

In general, we write quantities relevant to the primary SMBH without subscripts, those relevant to the secondary SMBH with a subscripted large black "dot", and those relevant to the stars with a subscripted star symbol. For example, the mass of the primary SMBH hole is written M , while those of the stars and secondary are written m_* and M_\bullet , respectively. Similarly the semi-major axes of any given star and the secondary are written a_* and a_\bullet . Note, however, that the subscript is foregone in figure labels. The mass ratio of the two SMBHs is denoted $q \equiv M_\bullet/M \leq 1$. We summarise the notation used in this work in table 1.

Because of the non-Keplerian potential (due to the stellar potential, the secondary SMBH and GR) there can be ambiguity when referring to the Keplerian orbital elements. We use unambiguous analogous quantities to the Keplerian orbital elements to describe the orbits of our stars. A star's semi-major axis, a_* , is defined to be a function of the star's energy, E ,

$$a_* \equiv \frac{GM}{2E}, \quad (1)$$

while the eccentricity is defined using the reduced angular momentum, L , and a_* :

$$e \equiv \sqrt{1 - \frac{L^2}{GMa}}. \quad (2)$$

In these expressions E and L are calculated in the primary SMBH's frame rather than the center of mass frame. These are the quantities shown in the figures unless stated otherwise.

Since in static non-Keplerian potentials L and E are conserved along orbits, then, provided the secondary's orbital period is long compared to a given star's, on the star's orbital timescale both a and e defined as above are well defined quantities and have minimal variations. Moreover, they are consistent with the standard definitions for the Keplerian orbital elements in the limit of Keplerian orbits.

The orbits which are interesting to us are those which approach the inner several Schwarzschild radii but have semi-major axes relatively close to the secondary SMBH; i.e., these orbits are highly eccentric. In this case,

$$L^2 \approx 2GMa(1 - e) \propto a(1 - e). \quad (3)$$

The right hand side of this equation is just the equation for the Keplerian periapsis distance in the limit of a Keplerian orbit. Because of this correspondence to both the angular momentum in these high eccentricity orbits and its correspondence to the periapsis distance in the Keplerian limit, we frequently plot $a(1 - e)$ and refer to it as the periapsis distance.

Stars whose angular momentum is less than $L_{\text{plunge}} \equiv 4GM/c$ on a close approach to a SMBH find themselves on a one-way trip to the black hole, 'plunging' across the event horizon. This corresponds to a periapsis distance in Schwarzschild radial coordinate of $4GM/c^2$ (see Eqn. 11), however in $a(1 - e)$, L_{plunge} corresponds to $8GM/c^2$.

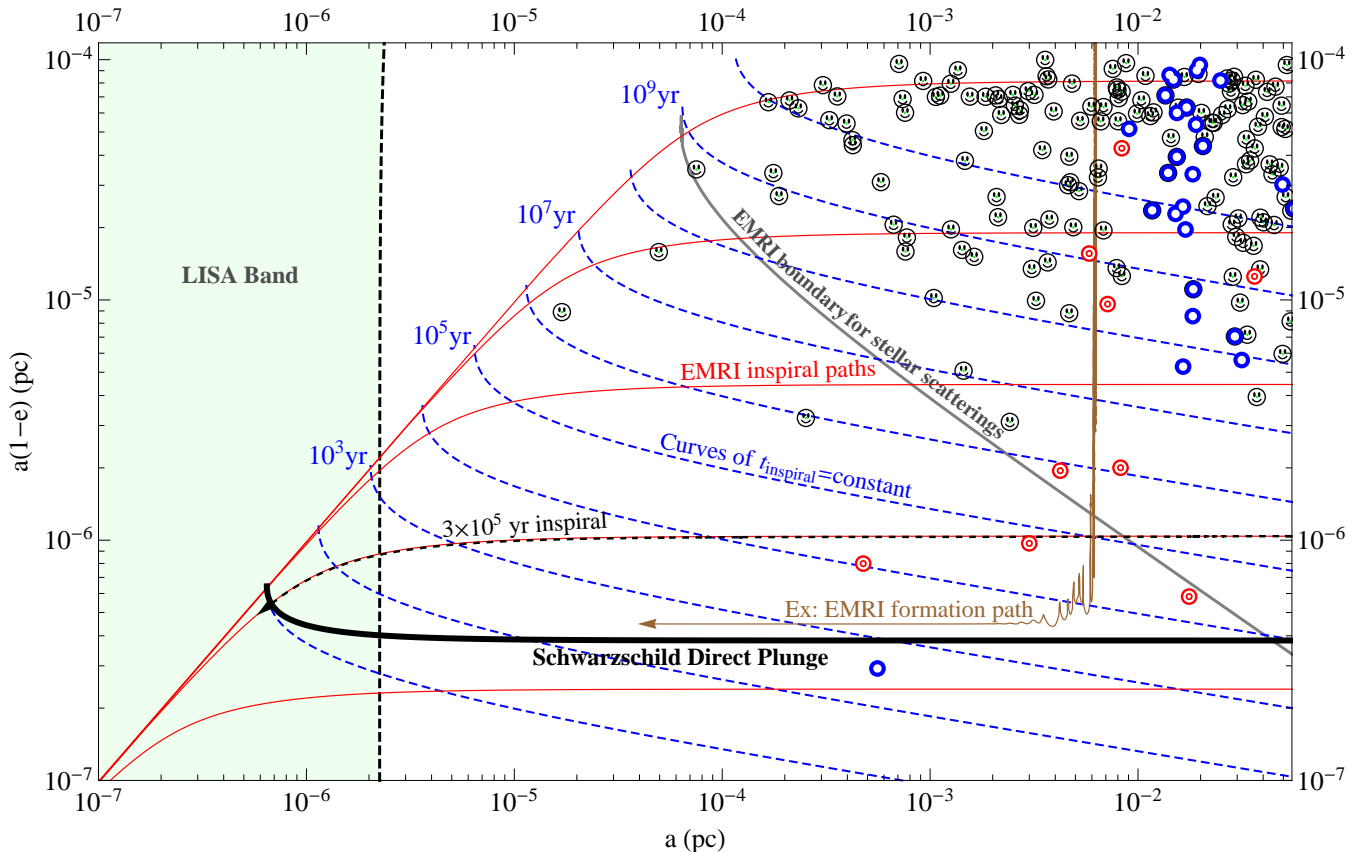


Figure 1. The standard EMRI parameter space with new addition: We plot $a(1-e)$ as a function of a with a and e defined by Eqns. 1 and 2, respectively. A compact object (stellar-mass black hole, neutron star, white dwarf) inspirals due to GW radiation along paths shown in solid red and approximated using the far-field equations of Peters (1964). The timescale for inspiral is approximately given by the times on the dashed blue curves, which are also calculated from Peters (1964). However, if no secondary SMBH is present and if the initial $\{a, a(1-e)\}$ pair lies above the solid gray line, the star is unlikely to complete its inspiral before two-body stellar scatterings move the orbit to larger $a(1-e)$. The minimum angular momentum a star can have while on a parabolic orbit without plunging into the primary SMBH, L_{plunge} (also referred to as the unstable circular orbit or separatrix), is plotted in thick solid black. In our simulation with mass ratio $q = 0.3$ and stellar masses $m_* = 10M_\odot$ the red targets are the initial conditions of a star which turned into an EMRI, the thick blue circles are the initial conditions for stars which turn into plunges, and the smiley faces are the initial conditions for stars who end the simulation uneventfully. We use the same initial conditions for all of our simulations, though which stars become EMRIs, plunges, or neither obviously differs. As an example of a star formed from the presence of a secondary SMBH we show in solid brown the path of one of the EMRIs produced in our simulations. The star is also marked as a red-outlined gold star in Figs. 4, 6, and 7 and used to demonstrate the importance of precession due to the stellar potential and GR in Fig. 3. This star has a path similar to many seen in our simulations, elucidating the new channel of EMRI production.

3 PHYSICAL SETUP

3.1 The Outline

Throughout this paper, the system we are considering is made up of three objects: 1) a primary SMBH surrounded by 2) a stellar cusp of mass equal to twice the primary's mass and 3) orbited by a secondary SMBH. We simulate this system by assuming that the stars in the cusp are non-interacting, allowing us to reduce the problem to a series of three-body problems which are made up of the primary SMBH, the secondary SMBH, and a star selected randomly from a stellar distribution.

In particular, we use a modified version of the simulation code used to study tidal disruptions in (Wegg & Bode 2011, hereafter WB11, see Sec. 4 for differences). There we were interested in the possibility of observing multiple tidal disruptions from the same galaxy due to the presence of a secondary SMBH. The similarities to the problem considered here make this code particularly appropriate.

We initially distribute stars isotropically according to an η -

model (Tremaine et al. 1994) for a single-mass stellar distribution around the primary SMBH (Sec. 3.3). However, we truncate the stellar potential just inside the stalling radius of the secondary (Sec. 3.4). The secondary is then spiraled inwards on a slightly eccentric orbit approximating the orbit of a SMBH evolving by dynamical friction and stellar ejection (Sec. 3.6), but smoothly stopping the inward motion at the stalling radius (Sesana, Haardt & Madau 2008). The primary difference between WB11 and here is that now we must take into account relativistic effects (Sec. 3.7) to properly model the stellar dynamics.

3.2 The Initial Conditions

We run four simulations, where we have varied two parameters: the SMBH mass ratio which is chosen to be either $q = 0.1$ or 0.3 and the stellar mass which is chosen to be either $1M_\odot$ or $10M_\odot$. The simulations are not independent, since we use the same initial velocities and positions for the 10^6 stars simulated in all of the simulations. This is significantly quicker computationally be-

Table 1. Notation: Equations and Descriptions of Parameters and Variables Listed in Alphabetical Order

Parameter	Description	Eqn. #
a_*	semi-major axis of a star	Eqn. 1
a_\bullet	semi-major axis of secondary SMBH	n/a
c	speed of light	n/a
e	eccentricity	Eqn. 2
E	specific orbital energy	Sec. 2.2
G	gravitational constant	n/a
i	inclination	n/a
L	total specific angular momentum	Eqn. 3
L_z	z component of specific angular momentum, SMBH binary lies in x - y plane	n/a
L_{plunge}	Angular momentum below which stars plunge into SMBH, equal to $4GM/c$	n/a
M	mass of primary SMBH	n/a
$M_*(< r)$	stellar mass interior to r	Eqn. 5
M_\bullet	mass of secondary SMBH	n/a
m_*	mass of secondary SMBH	n/a
P_*	period of star's orbit	n/a
P_\bullet	period of secondary SMBH's orbit	n/a
q	mass ratio of secondary to primary SMBH	n/a
r	radial position from primary SMBH	Sec. 3.3
r_c	characteristic size of cusp	Sec. 3.3
R_{Stall}	stalling radius of secondary	Sec. 3.6
T_{Kozai}	Kozai timescale	Eqn. 23
t_{Kozai}	instantaneous Kozai period	Eqn. 35
$t_{\phi, \text{GR}}$	time for orbit to precess by π radians due to GR	Sec. 6.4
$t_{\phi, \text{SP}}$	time for orbit to precess by π radians due to stellar potential	Sec. 6.4
$U(r)$	total gravitational potential	Eqn. 9
v	velocity	n/a
ΔL_b	oscillations in L_z on the timescale of the secondary SMBH's orbit	Sec. 6.6
ΔL_*	oscillations in L_z on the timescale of the stellar orbit	Sec. 6.7
η	parameter for cusp steepness	Sec. 3.3
ρ_*	density of stars	Eqn. 4
$\rho_*(< v)$	density of stars with velocity less than v	n/a

cause, for simulations with the same q , we only reintegrate orbits that pass within $100 GM/c^2$, the only region the stars' mass impacts its trajectory (which is only important when considering GR effects: see Sec. 4.2). Additionally, it also provides a direct comparison between the stars from each simulation which form EMRIs.

We choose a primary SMBH mass of $M = 10^6 M_\odot$ for all of our simulations since this will result in EMRIs with frequencies best suited for detection by low-frequency space-based gravitational wave detectors such as LISA (Amaro-Seoane et al. 2007) or eLISA (Amaro-Seoane et al. 2012). The 10^6 stars are given initial positions and velocities appropriate for a relaxed isotropic cusp centred on the primary SMBH (Sec. 3.3).

3.3 The Stellar Distribution

We integrate stars drawn from a cusp centred on the primary SMBH. The initial orbits of the stars are drawn from the self-consistent isotropic potential-density pair known as the η -model, meaning that the initial stellar distribution is drawn from (Tremaine et al. 1994, with $\mu = 0.5$)

$$\rho_*(r) = \frac{\eta}{2\pi r_c^3} \frac{M}{\left(\frac{r}{r_c}\right)^{3-\eta} \left(1 + \frac{r}{r_c}\right)^{1+\eta}}, \quad (4)$$

where r_c is the characteristic size of the cusp and η is a dimensionless parameter controlling the central steepness of the cusp. The stellar mass interior to radius r is therefore given by:

$$M_*(< r) \equiv M_{*,\eta}(< r) = \frac{2Mr^\eta}{(r_c + r)^\eta}. \quad (5)$$

Throughout this work we use $\eta = 1.25$ since this is the relaxed form of the distribution close to the SMBH (Bahcall & Wolf 1976). Our choice is motivated by Freitag, Amaro-Seoane & Kalogera (2006) who simulate multi-mass models of stellar cusps finding mass segregation close to the black hole. In that work the most massive species are steeper than $\eta = 1.25$ and less massive species less steep. However the overall density is close to $\eta = 1.25$.

We discuss the consequences of our assumption of a universal $\eta = 1.25$ in Sec. 7 and of mass segregation when calculating the rates in Sec. 5.2.

3.4 Stellar Distribution: Static, Fixed and Truncated

To reduce computational complexity we fix the stellar potential to the primary SMBH and do not evolve it in time. Though this is clearly inconsistent, since the secondary SMBH scatters stars onto new orbits and therefore modifies the stellar potential, most of our EMRIs are sourced from a tenth of the stalling radius where these modifications are not significant. We discuss this in more detail in Sec. 7.2 and demonstrate the magnitude of the error in Fig. 8.

However, without modification there would be a different inconsistency of much greater import. It is important that the pre-calculated SMBH path is consistent with the integrated test particle equations of motion. If an inconsistency is present then a particle orbiting close to the primary has an incorrect acceleration towards the secondary. This would represent an unphysical dipole-like perturbation, which would typically dwarf the smaller tidal quadrupole perturbation due to the secondary. An inconsistency of this type

would arise if Eqn. 5 was used as the stellar potential fixed to the primary, while the secondary orbit was calculated using Eqn. 7, where only the stellar mass interior to the secondary's orbit appears.

Instead, the stellar potential is truncated marginally inside the stalling radius. This has the result that the potential and stellar density are no longer self-consistent outside the stalling radius. However, stars outside the stalling radius that closely approach the SMBHs have undergone strong chaotic interactions with the binary. Therefore having a fully consistent stellar potential is less important in this region than for stars close to the primary which undergo secular interactions. For these inner stars we have the correct potential, and therefore the correct secular evolution.

3.5 Parameters of the Stellar Cusp

Throughout we use a fiducial cusp radius $r_c = 1.7$ pc. This is motivated by the fits from Merritt, Schnittman & Komossa (2009) to the inner regions of ACS Virgo Cluster galaxies (Côté et al. 2004). For power-law galaxies these give¹

$$r_{\text{inf}} = 22 (M/10^8 M_\odot)^{0.55} \text{ pc}, \quad (6)$$

where r_{inf} is defined such that the stellar mass interior to r_{inf} is $2M$, and M is the mass of the SMBH. Matching this to the η -model such that the central densities are equal gives $r_c = r_{\text{inf}}$. Extrapolating to Sgr A* which has a mass of $\approx 4 \times 10^6 M_\odot$ (Ghez et al. 2008) gives $r_{\text{inf}} = 3.8$ pc which agrees well with the observations of $r_{\text{inf}} \approx 4$ pc (Alexander 2005). Using $M = 10^6 M_\odot$ gives our fiducial $r_{\text{inf}} = r_c = 1.7$ pc.

We note that using a total stellar mass which is twice that of the primary SMBH has the convenient property that when matching the central density to a power law, r_c happens to be the radius at which the mass enclosed by the power law is $2M$ (the total stellar mass). This allows easy comparison with measurements.

3.6 The Inspiral of the Secondary

Initially the stars are on orbits consistent with the primary SMBH and the stellar potential. Subsequently their orbits are perturbed by interaction with the secondary SMBH as it inspirals to its stalling radius. In a fully self-consistent simulation the orbit of the secondary would evolve due to this exchange of energy with the stars. Instead, for efficiency and simplicity we calculate the orbit of the secondary SMBH assuming an inspiral dominated by dynamical friction with an appropriate Coulomb logarithm such that it stalls at the stalling radius.

Specifically, the secondary SMBH is, at time $t = 0$, given an eccentricity of approximately 0.1 and an initial separation equal to the cusp radius, r_c . It is then migrated inwards on a path governed by

$$\frac{d\mathbf{v}}{dt} = -\frac{G[M(1+q) + M_*(< r)]}{r^3} \mathbf{r} - \frac{\mathbf{v}}{t_{\text{df}}} \quad (7)$$

where $M_*(< r)$ is the stellar mass interior to r and

$$t_{\text{df}} = \frac{v^3}{2\pi G^2 \log\Lambda M q \rho_*(< v)} \quad (8)$$

characterises the dynamical friction (Binney & Tremaine 2008).

Here $\rho_*(< v)$ is the density of stars at r with velocity less than v . We have used a Coulomb logarithm that begins at $\log\Lambda \approx 4$, but which smoothly decreases to zero at the stalling radius calculated by Sesana et al. (2008). The functional form of the decrease was chosen to approximate the rate of shrinkage caused by the energy exchange with the stars during our simulations. This approximation was checked in WB11.

All the simulations in this work are all of length $45\sqrt{r_c^3/GM} \approx 1.5$ Myr. We assume that the secondary SMBH remains near its stalling radius for this duration. Our choice of simulation termination is arbitrary and was chosen to limit computation time: the rate of EMRIs and direct plunges has significantly dropped but not yet fallen to zero at the end of the simulations. We repeated one of the simulations for four times the duration to assuage fears that only a small fraction of the total number of EMRIs were captured. The number of events in this longer simulation suggested we have captured approximately $2/3$ of the total (for details see the more verbose Wegg 2013).

3.7 General Relativistic Effects

There are two important GR effects which must be accounted for: gravitational wave energy/angular-momentum losses and periastron precession. Ideally one would either integrate the exact equations of motion in full GR or use the simpler and well established post-Newtonian approximations. However, it is numerically prohibitive to attempt to use full GR, and the post-Newtonian expansions can be complex, are not separable, and do not have the appropriate divergences at low angular momenta. For example in the 3PN test particle limit the angular momentum at which parabolic orbits 'whirl' (i.e. precession diverges) around a Schwarzschild black hole is $L \approx 4.69 GM/c$ (compared to the correct value of $L = 4 GM/c$) and unphysical bound orbits can occur below this (Grossman & Levin 2009).

We instead choose the more straight forward approach of dealing with gravitational wave energy/angular-momentum losses and periastron precession separately in our symplectic integrator.

Recently, Wegg (2012) proposed several pseudo-Newtonian potentials appropriate for the periastron precession of test particles whose apoapses lies well beyond the Schwarzschild radius. We use potential B of that work, which balances both accuracy and computational cost.

As mentioned above, we deal with orbital energy and angular momentum losses due to gravitational wave emission separately. We deal with both by assuming the stars are on parabolic orbits. These losses are documented and fitting functions for the energy and angular momentum provided by Gair, Kennefick & Larson (2005). We use these fitting functions to determine the change in angular momentum and orbital energy during a complete periastron passage, and apply these losses discretely at periastron. The exact implementation is described in Sec. 4.2.

We note that for stars around Schwarzschild holes our methods remain accurate to arbitrary eccentricity (outside the exponentially narrow 'whirling' region just above $L = 4 GM/c$ where the precession will be underestimated). The simulations are terminated only if the angular momentum drops below $L \leq L_{\text{plunge}} = 4 GM/c$ as described in Sec. 4.4.

¹ D. Merritt, personal communication. From fitting to Fig. 2 of Merritt, Schnittman & Komossa (2009)

4 THE SIMULATION

To integrate the orbits of the test particles we utilise the symplectic integrator described in Preto & Tremaine (1999) and used in Peter (2008, 2009). We use this integrator because

- (i) Its symplectic nature causes energy to be conserved up to round-off error. This is desirable since spurious energy drifts would, over the many orbits simulated here, directly change the semi-major axis.
- (ii) With an appropriate choice of step size (see Sec. 4.3) orbits in a Keplerian potential are reproduced exactly with only a phase error which is $\mathcal{O}(N^{-2})$.

In particular, we use the version of the integrator used by WB11, extended to take into account both relativistic precession (Sec. 4.1) and the angular momentum and energy losses due to gravitational wave radiation (Sec. 4.2).

For a detailed discussion of the integrator used in WB11 see that work, and the works on which it was based (Preto & Tremaine 1999; Peter 2008, 2009). Here we discuss only how the integrator we use differs from that of WB11, along with checks (Sec. 4.3) and selection criteria (Sec. 4.4) relevant to this new context.

4.1 Pseudo-Newtonian potential

The prime reason we must use a pseudo-Newtonian potential to model relativistic precession is that the symplectic integrator is constructed by operator splitting and hence requires the Hamiltonian be separable. We therefore cannot evolve particles using post-Newtonian approximations in the equations of motion (as in e.g. Merritt et al. 2011a).

Instead, relativistic precession is included using the Pseudo-Newtonian potential labeled as ‘potential B’ in Wegg (2012). We use this potential since it accurately reproduces the precession of orbits with apoapsis in the far field (i.e. apoapsis $\gg GM/c^2$). Note that the potential of Paczyński & Wiita (1980) does not have this property. In addition, the precession correctly diverges as the orbit approaches L_{plunge} which separates bound orbits from plunges (this occurs at $L = 4GM/c^2$ for parabolic orbits). For reference the complete potential used is

$$U(r) = -\frac{GM}{r_1} \left(\frac{1}{1 - \frac{5}{6} \frac{r_{s,1}}{r_1}} + \frac{2}{3} \frac{r_{s,1}}{r_1} \right) - \frac{GM}{r_2} \left(\frac{1}{1 - \frac{5}{6} \frac{r_{s,2}}{r_2}} + \frac{2}{3} \frac{r_{s,2}}{r_2} \right) - V(r_1), \quad (9)$$

where the numerical subscripts 1 and 2 are used to distinguish quantities measured with respect to the primary and secondary, respectively, r_i is the distance to the i th SMBH, $r_{s,i}$ is the Schwarzschild radius of the i th SMBH, and $V(r_1)$ is the stellar potential produced by Eqn. 4.

4.2 Gravitational Wave Losses

When an object passes close to either SMBH, relativistic effects such as energy and angular momentum losses due to gravitational radiation become important. We incorporate these changes into the orbit by stepping out of the symplectic integrator at periapsis and calculating a new velocity vector when the star has passed within $100 GM/c^2$ of either SMBH. We note the calculations here are for non-spinning Schwarzschild black holes, this assumption is briefly discussed in Sec. 7.2.

Table 2. Coefficients for Eqn. 10

	$n = 0$	$n = 1$	$n = 2$
A_n^E	-0.318434	-5.08198	-185.48
B_n^E	0.458227	1645.79	8755.59
C_n^E	3.77465	-1293.27	-2453.55
A_n^L	-2.53212	-37.6027	-1268.49
B_n^L	0.671436	1755.51	9349.29
C_n^L	4.62465	-1351.44	-2899.02

The choice of $100 GM/c^2$ is motivated by the low losses for stars that remain outside this radius: For our highest mass ratio ($10M_\odot/10^6 M_\odot = 10^{-5}$) the loss of angular momentum per orbit for a parabolic orbit with periapsis $100 GM/c$ is $1.9 \times 10^{-8} GM/c$ and of energy is $1.6 \times 10^{-11} c^2$. For computational reasons (described below) the highest number of orbits integrated is 5×10^4 , and therefore losses for orbits which remain outside of $100 GM/c^2$ are negligible.

To compute the energy and angular momentum lost during a periapsis passage we assume the orbits are parabolic. We then relate the angular momentum in the orbit to the energy and angular momentum lost during each periapsis passage using the fitting functions for parabolic orbits from Gair, Kennefick & Larson (2006). In that paper they compute fitting functions to the energy and angular momentum loss using the Teukolsky equation. For convenience we provide these fitting functions here:

$$\begin{aligned} \frac{M}{m} \Delta X &= \cosh^{-1} \left[1 + B_0^X \left(\frac{4}{\tilde{r}_p} \right)^{N_X-1} \frac{1}{\tilde{r}_p - 4} \right] \\ &\times \sum_{n=0}^N A_n^X \left(\frac{1}{\tilde{r}_p} - \frac{4}{\tilde{r}_p^2} \right)^n \\ &+ \frac{\tilde{r}_p - 4}{\tilde{r}_p^{1+N_X/2}} \sum_{n=0}^N C_n^X \left(\frac{\tilde{r}_p - 4}{\tilde{r}_p^2} \right)^n \\ &+ \frac{\tilde{r}_p - 4}{\tilde{r}_p^{2+N_X/2}} \sum_{n=0}^{N-1} B_{n+1}^X \left(\frac{\tilde{r}_p - 4}{\tilde{r}_p^2} \right)^n, \quad (10) \end{aligned}$$

where X is either the specific energy E/c^2 or the (scaled) specific angular momentum $\tilde{L} = L/(GM/c)$, \tilde{r}_p is the periapsis distance in geometrized units, $N_E = 7$, $N_L = 4$, and the A_n^X , B_n^X , and C_n^X are coefficients given in Table 2. In Gair, Kennefick & Larson (2006) they note that $N = 2$ is sufficient for better than 0.2% accuracy everywhere. This is the order used in our code. Here, \tilde{r}_p is calculated based on the periapsis an orbit would have if it were parabolic and had the measured angular momentum:

$$\tilde{r}_p = \frac{\tilde{L}^2}{4} \left(1 + \sqrt{1 - \frac{16}{\tilde{L}^2}} \right). \quad (11)$$

Note that \tilde{r}_p is *not* calculated from the position of the star output by our simulation at its ostensible periapsis, since in the pseudo-Newtonian potential this does not match its relativistic value.

We subtract the energy and angular momentum loss given by Eqn. 10 at the step closest to periapsis. At this step we calculate a new velocity, v' , using the new specific energy, $E' = E + \Delta E$, and specific angular momentum, $L' = L + \Delta L$. Since the position is unchanged, the potential energy is unchanged and

$$v'^2 = v^2 + 2\Delta E. \quad (12)$$

The orbital plane remains unchanged for a Schwarzschild black

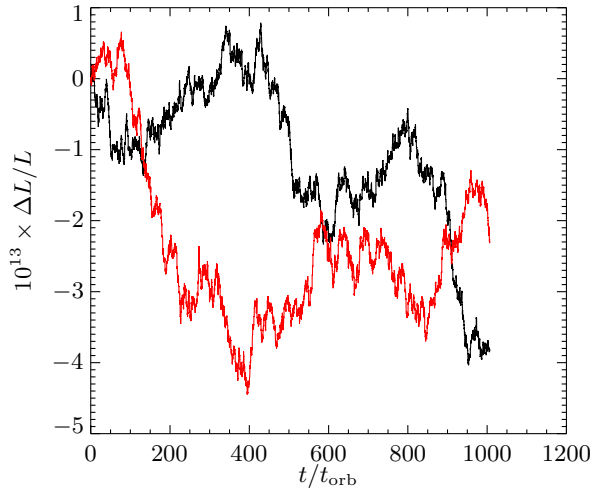


Figure 2. Plot showing the errors in conservation of reduced angular momentum, L , over many orbital periods (t_{orb}) of a high eccentricity ($e = 1 - 10^{-5}$) test particle. The red is without the procedure for calculating the change in \vec{v} at periapsis, while the black uses Eqn. 15 but with $\Delta L = 0$. The secondary has zero mass for both curves. The errors are still at the level $\Delta L/L \sim 10^{-12}$ indicating that the process of stepping in and out of the symplectic integrator does not inherently introduce significant errors.

hole and therefore

$$\vec{L}' = \frac{L + \Delta L}{L} \vec{L} = \vec{r} \times \vec{v}'. \quad (13)$$

Taking the dot product of this yields

$$\vec{r} \cdot \vec{v}' = \sqrt{L'^2 - r^2 v'^2} \quad (14)$$

where we take the positive branch of $\vec{r} \cdot \vec{v}'$ since this corresponds to the outgoing, post-periapsis solution. The cross-product $\vec{r} \times \vec{L}'$ yields

$$\vec{v}' = \frac{1}{r^2} \left[(\vec{r} \cdot \vec{v}') \vec{r} - \vec{r} \times \vec{L}' \right]. \quad (15)$$

Eqn. 15 together with 12, 13, and 14 are then used to calculate the new velocity \vec{v}' following the periapsis passage.

In Fig. 2 we show the numerical accuracy of this procedure by considering whether L remains constant over many orbits.

4.3 Step Size

Preto & Tremaine (1999) show that, for their adaptive symplectic integrator, in a Keplerian potential $U \propto 1/r$ then using a step size $\propto 1/r$ reproduces Keplerian orbits exactly with a phase error whose size is $\mathcal{O}(N^{-2})$, where N is the number of steps per orbit. Since the stars considered here usually evolve in a nearly Keplerian potential we therefore use a step size $\propto U$. The method of choosing the step size has not changed from WB11, except that here we have chosen to have 20,000 steps per orbit.

The phase error introduced by the finite step size in the integrator is along the orbit in a Keplerian potential i.e. a time error. The dominant error is also along the orbit for the pseudo-Newtonian potential. We expect both errors to be unimportant to both the dynamics and the rates, provided they are small per orbit.

Estimating both phase errors per orbit: (i) The phase error from using a finite step size in the integrator is of order $1/N^2 \sim$

10^{-8} . (ii) The phase error in using our pseudo-Newtonian potential compared to the geodesic equation is of order $E/c^2 = GM/ac^2$. Our EMRIs are sourced from the dynamics which occur at $a \sim 0.007$ pc. The phase error for these stars is therefore of order 7×10^{-6} per orbit.

These errors are also small per orbital period of the secondary SMBH. The pseudo-Newtonian potential accumulates a time error of order unity over the entire simulation at $a \sim 0.007$ pc. However we do not expect this to affect the dynamics.

To check that we are not sensitive to step size we re-ran a simulation with 10,000 steps per orbit. While individual stars evolved differently due to the chaotic nature of some orbits, the number of EMRIs and plunges were statistically unchanged.

4.4 Selection and Rejection

Throughout the stars' orbits their periapsis distances and semi-major axes were monitored. The simulation of a given star was stopped if one of three criteria were met: if the star was deemed an EMRI, a plunge, or beyond our computational capacity.

A star was labeled as an EMRI and its evolution terminated if it entered the (e)LISA band. We choose this to correspond to a semi-major axis where the test particle's orbital period is below 5000 s, i.e. when the semi-major axis is less than

$$a^3 < GM \left(\frac{5000 \text{ s}}{2\pi} \right)^2. \quad (16)$$

The results are not sensitive to this choice of stopping criteria.

A star's simulation was also stopped if the star's angular momentum at periapsis was less than the plunge angular momentum ($L \leq L_{\text{plunge}} = 4GM/c$). In this case the star was labeled as a plunge.

In both cases the star was subsequently reintegrated without a secondary to check that it would not otherwise have become an EMRI or plunge. In particular stars that over our simulation with no secondary, would have lost more than 5% of their energy to gravitational radiation, or have plunged into the primary hole are discarded and not included in the results.

Finally, due to computational limitations the stars' evolutions were limited to 10^{10} steps. This affects stars with semi-major axes less than 10^{-3} pc (see Figs. 7 and 8). These stars are both theoretically (see Sec. 6.8) and empirically (see Figs. 4 and 6) unlikely to form EMRIs.

5 RESULTS AND EMRI RATES

5.1 Introduction to Results and Rates

We provide a summary of the results of our simulations in Table 3, including both the total number of EMRIs produced and the implied probability of forming an EMRI given the simulation's parameters.

From Table 3 calculating the rates is straightforward: Given a species X of CO (stellar mass black hole, neutron star, or white dwarf) the simulation simulates N_* test particles and outputs the number of EMRIs $N_{\text{EMRI}}(X)$ assuming a mass m_X . Then

$$P_{\text{EMRI}}(X) \equiv N_{\text{EMRI}}(X)/N_* \quad (17)$$

is the probability that a star of species X eventually becomes an EMRI (Sec. 5.2).

We then multiply by the expected number of stars in our model

Table 3. Number of EMRIs and Their Probabilities in the Simulations

Sim #	Parameters				EMRI stars	
	q^a	$\frac{m_\star}{M_\odot} b$	N_\star^c	Duration (Myr) ^d	N_{EMRI}^e	P_{EMRI}^f
1	0.3	10	10^6	1.5	10	1.0×10^{-5}
2	0.3	1	10^6	1.5	1	0.1×10^{-5}
3	0.1	10	10^6	1.4	13	1.3×10^{-5}
4	0.1	1	10^6	1.4	3	0.3×10^{-5}

^a $q = M_\bullet/M$ is the ratio of the mass of the secondary SMBH to the primary SMBH.

^b The assumed mass of the stars in M_\odot . The mass of the stars is only relevant when the star passes within $100 GM/c^2$ of one of the SMBHs.

^c The total number of stars simulated during the run.

^d The duration of the simulation in megayears.

^e The total number of EMRIs formed during the simulation.

^f The probability of a CO of mass m_\star becoming an EMRI.

cusps of species X assuming some quantity of mass segregation (Sec. 5.3). This gives the approximate number of events for a given galaxy during the period of time that a secondary SMBH is settling to its stalling radius.

By determining the volumetric rate of galaxies undergoing a gasless merger, $\dot{n}_{\text{merger}}(M = 10^6 M_\odot)$ (Sec. 5.4), we may produce the predicted EMRI rate density (Sec. 5.5). That is,

$$\mathcal{R}_{\text{EMRI}}(X) = P_{\text{EMRI}}(X) N_X \dot{n}_{\text{merger}}(M = 10^6 M_\odot). \quad (18)$$

5.2 EMRI Merger Probability

Each of our simulations has $N_\star = 10^6$, with stars of mass $10 M_\odot$ or $1 M_\odot$ (but not both), where we use the former to predict the rates of stellar mass black holes and the latter to predict the rates for both neutron stars and white dwarfs. The probability that an object in a given simulation will turn into an EMRI is calculated using Eqn. 17 and shown in the final column of Table 3.

5.3 Species Number Density

The number of compact objects of type X expected as a function of position in the cusp is poorly understood, both observationally and theoretically (Hopman & Alexander 2006; O’Leary, Kocsis & Loeb 2009; Alexander & Hopman 2009). We note that mass segregation would not effect the migration of the binary we calculate in Sec. 3.6 (although overall density profiles different from $\eta = 1.25$ would). Since the details of mass segregation are uncertain, and most of the EMRIs initiate from a narrow range of semi-major axes, we choose a somewhat novel approach. When estimating the rates we assume the entire cusp at these radii is formed either of stellar mass BHs, or WDs and NSs. The reader can then scale the numbers to their preferred ratios of objects at $a \sim 0.01$ pc. This is possible since in the case considered the rates scale linearly with number of COs. Our fiducial choice here is to scale to the degree of segregation found by Freitag, Amaro-Seoane & Kalogera (2006). We tabulate these values in column b of Table 4 and use them as our fiducial values.

To determine the number of each stellar remnant in the cusp we must first consider stellar-mass black holes. In Freitag, Amaro-Seoane & Kalogera (2006) they find that there is roughly 10 times as much mass in SBHs than in MSSs close to the SMBH. We assume here that SBH masses are $10M_\odot$, which then tells us that

there are roughly the same number of SBHs as there are MSSs in the cusp. Because most of the mass in the cusp is from the SBHs we can approximate the total number of SBHs by dividing the total mass of the cusp, which we have assumed to be $2 \times 10^6 M_\odot$, by the mass of the SBHs. This yields 2×10^5 stellar-massed black holes in the cusp. This then tells us there are roughly 2×10^5 MSSs.

As with stellar-massed black holes Freitag, Amaro-Seoane & Kalogera (2006) provides the mass density ratios of each stellar type to that of MSSs. Therefore, assuming that NSs and WDs are roughly $1M_\odot$, it is trivial to determine the number of each species in the cusp relative to the number of MSSs. Multiplying by N_{MSS} then gives the total number of each species in the cusp:

$$N = \begin{cases} 2 \times 10^5 & \text{for main sequence stars} \\ 2 \times 10^5 & \text{for stellar-mass black holes} \\ 2 \times 10^4 & \text{for neutron stars} \\ 6 \times 10^4 & \text{for white dwarfs} \end{cases}. \quad (19)$$

These calculations are summarized in column d of Table 4.

The predicted number of stellar-massed BHs in Table 4 implies an unrealistic total number of stellar-massed BHs in the cusp, but these numbers have been scaled to ensure the correct number of stellar-massed BHs in the inner cusp, from where the EMRIs are sourced. Thus, these numbers produce the correct number of stellar-massed BHs in the relevant region.

5.4 Number Density of Mergers

We approximate the number density of mergers of SMBHs of mass $10^6 M_\odot$ and mass ratios between 0.1 and 0.3 by determining the number density of SMBHs of mass $(10^{5.5} - 10^{6.5}) M_\odot$ and assuming one such SMBH merger per galaxy lifetime.

Aller & Richstone (2002) find a local number density of SMBHs with mass $(10^{5.5} - 10^{6.5}) M_\odot$ of $4 \times 10^6 \text{ Gpc}^{-3}$ (assuming $H_0 = 70 \text{ km s}^{-1} \text{ Mpc}^{-1}$). Therefore we approximate,

$$\dot{n}_{\text{merger}}(M = 10^6 M_\odot) \sim 3 \times 10^{-4} \frac{\text{mergers}}{\text{Gpc}^3 \text{ yr}}. \quad (20)$$

We have tacitly assumed above that mergers happen uniformly in time. The assumed constant merger rate (of one merger per galaxy) will probably be fairly accurate for a LISA or a LISA-like experiment able to detect EMRIs to redshift $z \sim 1$. However because of the locally falling merger rate they would be over estimates if, for example, EMRIs are detectable only to redshifts of

Table 4. Approximate Mass and Number Densities of Species Deep (< 0.05 pc) in Stellar Cusp found by (Freitag, Amaro-Seoane & Kalogera 2006).

Species X	$\frac{m_X}{M_\odot} a$	$\frac{\rho_X}{\rho_{\text{MSS}}} b$	$\frac{N_X}{N_{\text{MSS}}} c$	$N_X d$
Main Sequence Star	1	1	1	2×10^5
Stellar-Mass Black Hole	10	~ 10	~ 1	2×10^5
Neutron Star	1	~ 0.1	~ 0.1	2×10^4
White Dwarf	1	~ 0.3	~ 0.3	6×10^4

^a Mass of species X in solar masses.

^b Ratio of density of species X to that of main sequence stars in the region where EMRIs are formed in our simulations (Freitag, Amaro-Seoane & Kalogera 2006).

^c Ratio of number of stars of species X to the number of main sequence stars in the region where EMRIs are formed in our simulations.

^d Total number of species X in the entire stellar cusp if the cusp were to have the same ratio of species X to main-sequences stars as in the region where the EMRIs are sourced in our simulation.

$z \sim 0.1$. However there are large uncertainties both in the design of any LISA like mission, the detectability of EMRIs, and the cusps and the degree of their relaxation and segregation around $10^6 M_\odot$ SMBHs. The SMBH merger rates used here are chosen due to their simplicity given these uncertainties.

5.5 Final Rates

The rate of EMRI production per unit volume, $\mathcal{R}_{\text{EMRI}}$, is calculated using Eqn. 18. We use the probability that each star in our simulations becomes an EMRI, P_{EMRI} , from Table 3, the numbers of each species, N_X , from Table 4, and the SMBH merger rate, \dot{n}_{merger} , from Eqn. 20.

This analysis ultimately yields the following rates

$$\mathcal{R}_{\text{EMRI}}(q = 0.1) = \begin{cases} 8 \times 10^{-4} \text{ yr}^{-1} \text{ Gpc}^{-3} & \text{for SBHs} \\ 2 \times 10^{-5} \text{ yr}^{-1} \text{ Gpc}^{-3} & \text{for NSs} \\ 5 \times 10^{-5} \text{ yr}^{-1} \text{ Gpc}^{-3} & \text{for WDs} \end{cases} \quad (21)$$

and

$$\mathcal{R}_{\text{EMRI}}(q = 0.3) = \begin{cases} 6 \times 10^{-4} \text{ yr}^{-1} \text{ Gpc}^{-3} & \text{for SBHs} \\ 6 \times 10^{-6} \text{ yr}^{-1} \text{ Gpc}^{-3} & \text{for NSs} \\ 2 \times 10^{-5} \text{ yr}^{-1} \text{ Gpc}^{-3} & \text{for WDs} \end{cases} \quad (22)$$

For reference these rates are given in Table 5.

For context our overall detection rates are significantly lower than the $\mathcal{R} \sim 1 \text{ yr}^{-1} \text{ Gpc}^{-3}$ predicted from isolated SMBHs by Gair et al. (2004). We note that there is presently considerable uncertainty in each rate estimate, and show in Sec. 7.1 that the rate given here has the prospect of being astrophysically interesting to LISA-like missions.

6 STELLAR DYNAMICS: UNDERSTANDING OUR EMRIS AND PLUNGES

The processes which produce the majority of our EMRIs are, dynamically, quite rich. In particular, the interplay between the physical processes of the secular Kozai effect, the SP precession, the competing GR precession, and the oscillations of the orbital elements on the secondary SMBH's orbital timescale is physically intricate and interesting. We elucidate these effects in this section, where we first give a brief description of the Kozai effect (Secs. 6.1 and 6.3), then discuss various complicating effects individually

(Secs. 6.4–6.7), and finally consider the different effects together elucidating their relevance to the EMRI rates (Sec. 6). Of particular importance are the oscillations in the angular momentum on the timescale of the secondary (Sec. 6.6).

6.1 Kozai Effect — Historical Formalism

Instead of giving a detailed description of the Kozai mechanism, something already comprehensively elucidated by the original papers (Lidov 1962; Kozai 1962) and much subsequent work (Holman, Touma & Tremaine 1997; Blaes, Lee & Socrates 2002; Ivanov, Polnarev & Saha 2005; Thompson 2011) in various different contexts, we aim to provide in this section the key equations and their consequences relevant to our problem.

In our circumstances the Kozai mechanism is a secular process whereby the weak quadrupolar tidal force from the secondary SMBH perturbs the orbits of stars around the primary SMBH.

The original theory (Lidov 1962; Kozai 1962) of the Kozai mechanism assumed (in the context of our problem) not only that the semi-major axis of the star is significantly less than that of the secondary SMBH, but also that the star is on what would otherwise be a Keplerian orbit in the absence of the secondary (i.e., general relativistic effects along with effects due to the stellar potential are ignored). Moreover, the Kozai-Lidov theory assumes a purely quadrupolar force and averages over the orbits of both the star and the secondary SMBH. Throughout this subsection we retain these assumptions.

Here, as with elsewhere in this paper, we will use the following conventions: ω is the argument of periapsis, χ is the longitude of the ascending node, P_\bullet is the period of the secondary, P_\star is the radial period of the star, and

$$T_{\text{Kozai}} \equiv \frac{2}{3\pi q} \frac{P_\bullet}{P_\star} P_\bullet = \frac{4}{3q} \left(\frac{a_\star}{a_\bullet} \right)^{-3/2} \sqrt{\frac{a_\bullet^3}{GM}} \quad (23)$$

is the widely discussed characteristic timescale on which the Kozai oscillations occur (e.g., Ivanov, Polnarev & Saha 2005).

Starting from the exact equations of motion in the osculating elements, written with the true anomaly as the independent variable, and averaging over both the orbits of the star and the secondary SMBH, Lidov (1962) obtained an insightful set of differential equations (written in the form of Ivanov, Polnarev & Saha

Table 5. Final Rates of EMRIs Due To SMBH Binaries

q^a	$\mathcal{R}_{\text{EMRI}} (\text{yr}^{-1} \text{Gpc}^{-3})^b$		
	SBH	NS	WD
0.3	6×10^{-4}	6×10^{-6}	2×10^{-5}
0.1	8×10^{-4}	2×10^{-5}	5×10^{-5}

^a The mass ratio of the secondary SMBH to the primary

^b Rate of EMRIs due to SMBH binaries for the cases of stellar-mass black holes (SBHs), neutron stars (NSs), and white dwarfs (WDs) assuming that all mergers at rate \dot{n}_{merger} have mass ratio q

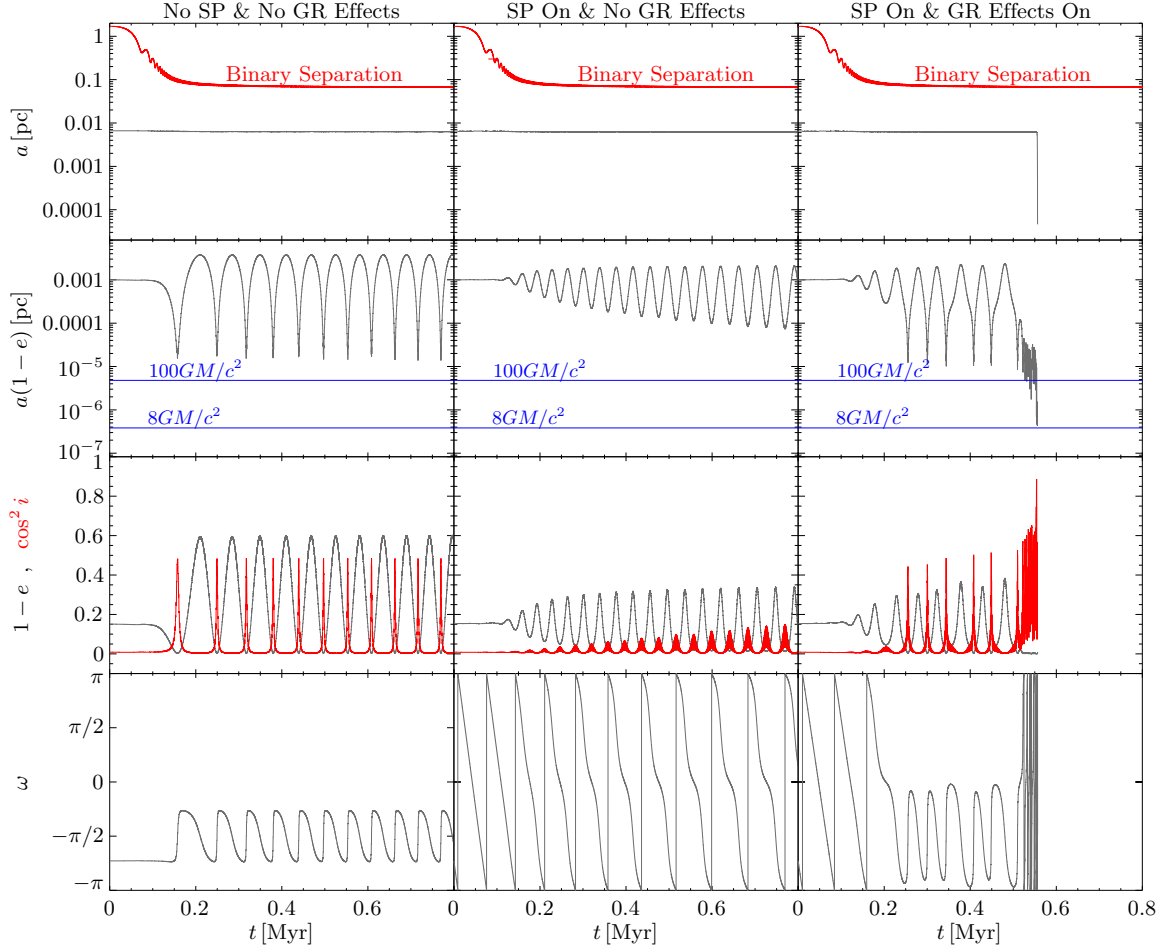


Figure 3. Comparison of Kozai features for a star which turned into an EMRI in one of our simulations evolved with different forms of precession: in the first column we follow the star without any form of precession (no SP or GR precession), in the second column we “turn on” SP precession and in the third column we show the results of the full integration which also has GR precession and GW energy loss. Describing the rows of the plot: In row 1 we plot in charcoal the semi-major axis of a $10 M_{\odot}$ star (the mass is only relevant when GR effects are considered; final column) as a function of time along with the position of the secondary plotted in red. In row 2 we plot $a(1 - e)$ in charcoal as a function of time. Also plotted are the lines of constant $a(1 - e) = 8 GM/c^2$ and $100 GM/c^2$, the latter being the arbitrary radius where we start calculating the energy loss for the orbit (see Sec. 4). In row 3 we plot $1 - e$ in charcoal and $\cos^2 i$ in red as a function of time. The product of the two is proportional to L_z^2 which is a conserved quantity in the standard Kozai formalism. In the final row we plot the argument of periastron as a function of time. From left to right there are clear changes in the star’s orbit as new forms of precession are added: In the first column once the secondary has reached the stalling radius the star undergoes librating oscillations about $\omega = -\pi/2$ most akin to the traditional Kozai oscillations as described in Sec. 6.1. In the second column three clear changes occur: the star begins retrograde precession (row 4) as the SP precession dominates, the oscillation period decreases (rows 2, 3 and 4), and the magnitude of the oscillations is reduced (rows 2 and 3). In the final column (with SP and GR effects on) a very different phenomenon occurs which can be separated into three regions: strong retrograde precession due to the stellar potential, a librating mode in a pseudo-Kozai oscillation where SP and GR precession loosely cancel, and a final phase marked by rapid, and apparently chaotic, prograde precession driven by GR. Again, the period of oscillations in e and i are half the precession period. The increasing relevance of GR precession is due not only to having a lower periastris distance, but also to the effects of the SP being weaker as the eccentricity grows. This star is also marked as a red-outlined gold star in Figs. 4, 6, and 7.

2005):

$$T_{\text{Kozai}} \frac{da}{dt} = 0 \quad (24)$$

$$T_{\text{Kozai}} \frac{de}{dt} = -\frac{5}{2} e \sqrt{1-e^2} \sin^2 i \sin 2\omega \quad (25)$$

$$T_{\text{Kozai}} \frac{di}{dt} = -\frac{5}{4} \frac{e^2 \sin(2i) \sin(2\omega)}{\sqrt{1-e^2}} \quad (26)$$

$$T_{\text{Kozai}} \frac{d\omega}{dt} = \frac{2(1-e^2) + 5 \sin^2(\omega)(\cos^2 i - (1-e^2))}{\sqrt{1-e^2}} \quad (27)$$

$$T_{\text{Kozai}} \frac{d\chi}{dt} = -\frac{\cos i}{\sqrt{1-e^2}} \{1 + e^2(5 \sin^2 \omega - 1)\}. \quad (28)$$

The primary characteristic of the Kozai mechanism is that the star's orbital elements undergo an oscillatory motion which has a period given approximately by T_{Kozai} , and which can be of significant magnitude. There are several key outcomes from the above equations:

- (i) a , and, therefore, the energy of the star's orbit remains constant (Eqn. 24).
- (ii) The eccentricity and inclination reach their extremal values only when $\omega = 0, \pm\pi/2, \text{ or } \pi$ (solving Eqn. 25 equal to 0).

In addition to a , equations 24-28 admit two further integrals of the motion (Lidov 1962; Kozai 1962):

$$\Theta = (1 - e^2) \cos^2 i \quad \text{is conserved and} \quad (29)$$

$$Q = e^2 [5 \sin^2 i \sin^2 \omega - 2] \quad \text{is conserved,} \quad (30)$$

which together tell us several things about a star's evolution:

- (iii) The z component of the angular momentum is conserved since $L_z = \sqrt{GMa\Theta}$ (Eqn. 29).
- (iv) All solutions have $1 - e^2 \geq \Theta$ or, equivalently, $e < \sqrt{1 - \Theta}$ (Eqn. 29).
- (v) The eccentricity reaches its maximum (minimum) when the inclination reaches its minimum (maximum) (Eqn. 29).

Many of these points can be seen in the first column of Fig. 3, where we have plotted the evolution of a star whose fate in our $q = 0.3$ and $m_* = 10 M_\odot$ simulation was to become an EMRI (also shown in Figs. 1, 4, 6, and 7), except with the stellar potential and GR effects turned off. While the semi-major axis of the star remains constant (first row), L goes through significant oscillations. To avoid confusion we reiterate that in our simulations we are not solving Eqns. 24–28, but rather directly integrating the full three-body (non-orbit averaged) calculation (see Sec. 4 for detailed explanation).

6.2 Conservation of L_z in Standard Kozai-Lidov Formalism

Point (iii) above has particular importance to our problem. Since L_z is conserved, it must be true that $L \geq L_z$ through out the evolution of a star. Because EMRIs, tidal disruptions, or plunges all require a low total angular momentum of order L_{plunge} or smaller, if a star is to be driven to be an EMRI, tidal disruption, or plunge by the Kozai mechanism then we require $L_{\text{plunge}} \gtrsim L > L_z$. That is, according to the standard Kozai-Lidov formalism, for Kozai to drive a star to plunge, it must be true that

$$L_z \lesssim L_{\text{plunge}}. \quad (31)$$

Stars with L_z fulfilling this condition are said to lie inside the Kozai wedge (Chen et al. 2009).

The importance of this point is illustrated in Fig. 4 where we

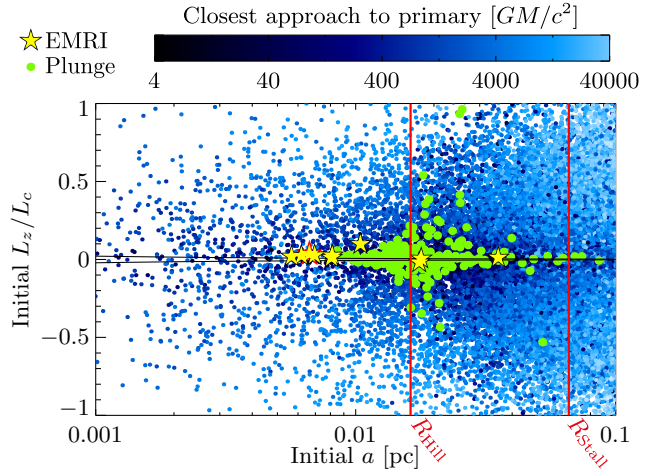


Figure 4. We plot the initial L_z/L_c of our stars as a function of the initial semi-major axis, a . L_c is the circular angular momentum: $L_c^2 = GMa$. In the Kozai formalism (Sec. 6.1) L_z and a are conserved over a star's evolution. The final stalling radius of the secondary is shown as a vertical red line. The simulation shown has $q = 0.3$ and $m_* = 10 M_\odot$. We encode the shortest distance to the primary SMBH a star reached over its evolution by colour: gold stars represent stars which have turned into EMRIs (Sec. 4.4), green dots are stars which have plunged into the primary SMBH, and all other stars are coloured in shades of blue with darker blues being shorter distances (see legend, calculated using Eqn. 11). Also plotted in solid black is the Kozai “wedge”; lines of $L_z = \pm 4 GM/c$. Inside these lines the standard Kozai formalism (Sec. 6.1) predicts that it is possible, but not necessary, that a star reaches $L = 4 GM/c^2$. Thus, it is only inside these wedges that the standard Kozai formalism would predict plunges. Though this condition is not met for the majority of plunges/EMRIs, the clustering around small L_z and at semi-major axes much smaller than the innermost position of the secondary indicate that the Kozai mechanism is important. That many EMRIs and plunges lie outside the Kozai wedge is primarily due to the oscillations on the orbital timescale of the secondary SMBH (see Sec. 6.6), and is demonstrated in greater detail in Fig. 6.

plot the outcomes of all stars in the simulation with $q = 0.3$ and $m_* = 10 M_\odot$ as a function of their initial L_z/L_c and a , where L_c is the circular angular momentum. Most plunges and EMRIs originate far from the secondary and come from a relatively narrow region of L_z/L_c , indicating that the Kozai mechanism is important to their evolution.

However, the standard Kozai formalism does not explain the distribution of plunges, and EMRIs, in L_z/L_c . To illustrate this in Fig. 4 we plot the Kozai wedge (lines $L_z = \pm 4 GM/c$). The reason that most EMRIs and plunges are initially outside (but close to) the Kozai wedge is explained in Sec. 6.6.

Note that Lithwick & Naoz (2011) and Katz, Dong & Malhotra (2011) have recently shown non-conservation of L_z by the Kozai effect for the restricted three body case due to the octupole term in the perturbation expansion. In our simulations however, the secondary stalls with a low eccentricity ($e \sim 0.03$), and therefore the octupole term does not secularly perturb the orbit on the timescales simulated. They may however be important on longer timescales and with higher eccentricity perturbers.

6.3 Kozai Effect — Instantaneous Kozai Timescale

In addition to the Kozai timescale, T_{Kozai} , we define a second ‘instantaneous Kozai timescale’, t_{Kozai} . T_{Kozai} is the characteristic timescale describing the total period of of a Kozai oscillation. We

define t_{Kozai} to be the time that it takes for the orbital angular momentum of the star to change by its own magnitude. Thus, it allows one to understand the relevant timescale for change during an oscillation. This is particularly useful for understanding when GR precession truncates an oscillation at high eccentricity.

The instantaneous Kozai-Lidov timescale is, to order unity, given by (Chen et al. 2011)

$$\frac{1}{t_{\text{Kozai}}} \sim \frac{1}{L} \frac{dL}{dt}, \quad (32)$$

where the specific angular momentum is given by

$$L = \sqrt{GMa_*(1-e^2)}, \quad (33)$$

and the torque due to the quadrupolar tidal force from the secondary is

$$\left| \frac{d\vec{L}}{dt} \right| = \left| \vec{F} \times \vec{r} \right| \sim \frac{qGMa_*^2}{a_*^3}. \quad (34)$$

Together Eqns. 32–34 give an instantaneous Kozai timescale of

$$t_{\text{Kozai}} \sim \frac{\sqrt{1-e^2}}{2\pi q} \left(\frac{a_\bullet}{a_*} \right)^3 P_* \quad (35)$$

$$\sim \frac{\sqrt{1-e^2}}{2\pi q} \frac{P_*^2}{P_*}. \quad (36)$$

Up to a constant and the factor $\sqrt{1-e^2}$ this is the standard Kozai timescale given by Eqn. 23. The non-constant factor $\sqrt{1-e^2}$ shows that the timescale for change in the angular momentum is shorter during periods of high eccentricity. This is because during periods of high eccentricity the orbit has the lowest angular momentum, requiring smaller torques to be significantly altered.

6.4 Apical Precession

When any form of apical precession becomes comparable to t_{Kozai} , then the magnitude of the Kozai oscillations is inhibited. This process is sometimes referred to in the literature as the Kozai mechanism being ‘de-tuned’ (e.g. Thompson 2011). In our context there are two relevant forms of precession which affect the Kozai mechanism: that due to the stellar potential, and that due to GR precession.

The precession due to the non-Keplerian stellar potential results in an apical precession per stellar orbit of approximately (e.g. Merritt et al. 2011a)

$$\delta\omega_{\text{SP}} \sim -2\pi \frac{\sqrt{1-e^2}}{1+\sqrt{1-e^2}} \frac{M_*(< a_*)}{M}. \quad (37)$$

Hence, the timescale to precess though π radians is

$$t_{\phi, \text{SP}} \equiv \left| \frac{\pi}{\delta\omega_{\text{SP}}} \right| P_* \sim \frac{1}{2} \frac{1+\sqrt{1-e^2}}{\sqrt{1-e^2}} \frac{M}{M_*(< a_*)} P_*. \quad (38)$$

The mass ratio depends on the cusp model as discussed in Sec. 3.3.

On the other hand, GR precession has a different dependence. In the far field limit, the per orbit GR precession of a star is given by

$$\delta\omega_{\text{GR}} = \frac{6\pi GM}{c^2 a_*(1-e^2)} = \frac{3\pi}{1-e^2} \frac{r_{\text{S}}}{a_*}. \quad (39)$$

Then, the timescale to precess through π radians is given by

$$t_{\phi, \text{GR}} = \left| \frac{\pi}{\delta\omega_{\text{GR}}} \right| P_* = \frac{1}{3} (1-e^2) \frac{a_*}{r_{\text{S}}} P_*. \quad (40)$$

It is important to note both that GR precession and SP precession are in opposite directions (Eqns. 37 and 39) and that as the eccentricity of a star’s orbit grows, $t_{\phi, \text{SP}}$ increases while $t_{\phi, \text{GR}}$ decreases (Eqns. 38 and 40).

We can see the individual effects in Fig. 3 where, in the first column we plot the orbital parameters for the example star without either the effects of the stellar potential or GR, in the second column we plot the evolution including only the stellar potential, and in the third column we show the evolution of the full simulation with both the stellar potential and GR effects. One sees that in this case without the GR effects included the stellar potential largely damps the Kozai oscillations, while when they are included the star still reaches the angular momentum expected from the traditional Kozai formalism.

6.5 Extreme Apical Precession

When some non-Keplerian effect, other than Kozai, causes orbital precession on a timescale $t_{\phi, \text{ext}} \equiv \frac{2\pi}{\dot{\omega}_{\text{ext}}}$ which is much shorter than T_{Kozai} , then the standard Kozai cycles are truncated on this new shorter timescale. Because $t_{\phi, \text{ext}} \ll T_{\text{Kozai}}$, the argument of periastris ceases to evolve according to Eqn. 27, and instead follows an evolution dictated by this exterior effect (i.e., $\omega(t) \approx \int \dot{\omega}_{\text{ext}} dt$). The $\sin 2\omega$ term in the evolution of e and i (Eqns. 25 and 26) mean that both e and i will undergo two oscillations over a time $t_{\phi, \text{ext}}$, as expected for the quadrupole perturbation induced by the secondary.

Moreover, given a star with eccentricity e and angular momentum $L(e)$ this reduces the amplitude of the Kozai oscillations to roughly

$$\Delta L \sim L(e) \frac{t_{\phi, \text{ext}}}{t_{\text{Kozai}}}. \quad (41)$$

That is, stars with low eccentricities will continue to have low eccentricity, but stars with high eccentricity retain their high eccentricity.

In the latter case, if a star reaches a high enough eccentricity that GR precession alone causes the orbit to precess significantly (e.g., by π radians) before the angular momentum can change significantly (e.g., by its own magnitude) then the Kozai oscillations will be stalled at high eccentricity. When this occurs can be found by taking the ratio of $t_{\phi, \text{GR}}$ to t_{Kozai} ,

$$\frac{t_{\phi, \text{GR}}}{t_{\text{Kozai}}} \sim 2\sqrt{2}q \left(\frac{a_\bullet}{a_*} \right)^3 \frac{a_*}{r_{\text{S}}} \sqrt{1-e}, \quad (42)$$

and solving for $1-e$

$$1-e = \frac{1}{8} \frac{1}{q^2} \left(\frac{a_\bullet}{a_*} \right)^6 \left(\frac{r_{\text{S}}}{a_*} \right)^2. \quad (43)$$

This has been referred to as the Schwarzschild barrier in the context of resonant relaxation around single SMBHs by Merritt et al. (2011a). In the case of our example star (shown in Figs. 1, 3, 4, 6, and 7) this limit to the eccentricity occurs when $1-e \approx 3 \times 10^{-4}$. In fact, this star does reach this eccentricity, subsequently ceases to oscillate, and forming an EMRI on a timescale too short to be clearly visible in Fig. 3.

Thus the example star highlights that the case of high eccentricity is of particular importance, since retaining high eccentricity accelerates the rate at which a star inspirals due to GW radiation.

6.6 Fluctuations in L_z on the orbital timescale of the SMBH binary²

In the standard Kozai mechanism, when averaged over the timescale of the SMBH binary, the component of angular momentum perpendicular to the binary's orbit, L_z , is conserved. However, on shorter timescales this is not the case. This is because the symmetry about the z -axis is broken on shorter timescales.

To illustrate this consider a short period over which the secondary SMBH moves negligibly: in this case the symmetry axis of the quadrupolar tidal force on the star is directed towards the secondary (*not* in the z direction). Therefore, it is this component of the angular momentum (which is perpendicular to z) that is conserved on very short timescales.

The resultant size of the fluctuations over the binary orbital period will be of order³

$$\Delta L_b \sim \frac{dL}{dt} \frac{P_\bullet}{4} \quad (44)$$

where the factor of 4 is to approximately take account of the dominant quadrupolar force, which gives rise to four reverses in sign per orbital period, P_\bullet . Using the previously calculated torque (Eqn. 34) we find

$$\Delta L_b \sim \frac{qGMa_\star^2}{a_\bullet^3} \frac{P_\bullet}{4} = \frac{\pi}{2} q \left(\frac{a_\star}{a_\bullet} \right)^{3/2} \sqrt{GMa_\star}, \quad (45)$$

$$\equiv \frac{\pi}{2} q \left(\frac{a_\star}{a_\bullet} \right)^{3/2} L_c, \quad (46)$$

so that

$$\Delta(1-e) = \frac{\Delta L_b}{L_c} = \frac{\pi}{2} q \frac{P_\star}{P_\bullet}. \quad (47)$$

Here $L_c = \sqrt{GMa_\star}$ is the maximum angular momentum with semi-major axis a_\star , the circular angular momentum.

The fluctuations in ΔL_b become vitally important when $\Delta(1-e) \lesssim 1-e$.

$$1-e \lesssim \frac{\pi}{2} q \frac{P_\star}{P_\bullet} = \frac{\pi}{2} q \left(\frac{a_\bullet}{a_\star} \right)^{3/2}. \quad (48)$$

This requirement is analogous to requiring that the variations in the periapsis distance due to the ΔL_b are comparable to the periapsis distance.

If the condition $\Delta(1-e) \lesssim 1-e$ is violated then the secular approximation breaks down. Therefore, whenever the secular Kozai equations are used, it is important to check that, at the highest eccentricities of interest, the size of the oscillations in eccentricity.

We demonstrate this effect in Fig. 5. There we plot $1-e$ for a minimum of $a_\star(1-e)$ in column 1 of Fig. 3 as a function of time. In this case the star is being evolved without the effects of GR or precession due to the stellar potential so as to best illustrate the effect. In red is the approximate path predicted by the Kozai formalism, Eqns. 24–28, and in green is the predicted envelope given by Eqn. 48. Each dot represents the calculated value of $1-e$ at periapsis during the integration.

The importance of these oscillations to the evolution of stars

² We note that an earlier version of this manuscript was shared with Antognini et al. (2013) and Katz & Dong (2012) who then nicely showed this effect can be important in hierarchical triples (Antognini et al. 2013), and mergers of white dwarfs in particular (Katz & Dong 2012).

³ A more precise but complex calculation of ΔL_b can be found in Appendix B of Ivanov, Polnarev & Saha (2005).

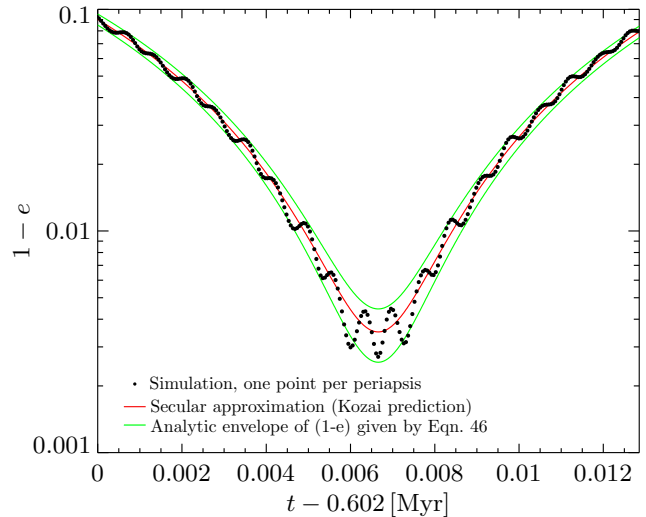


Figure 5. We plot $1-e$ as a function of time across the peak of the oscillation in eccentricity. In red is the approximate value predicted by the standard Kozai formalism (averaged over the secondary's orbit, Eqns. 24–28), while in green is the expected envelope of oscillations in $1-e$ over the secondary's orbital timescale given by Eqn. 48. Each dot represents the value of $1-e$ calculated by our simulation at apoapsis during the first maximum of the eccentricity in the simulation shown in the first column of Fig. 3 (in which both the stellar potential and the relativistic precession were turned off for clarity). The orbital modulations at the period of the secondary can be significant in these regions.

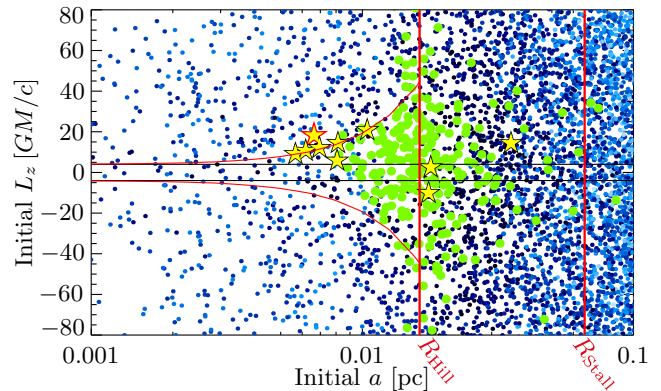


Figure 6. We plot the initial L_z as a function of the stars' initial semi-major axes. The symbols and data sets are the same as in Fig. 4. Here we also show in red $L_{\text{plunge}} + \Delta L_b$ where ΔL_b are the range of possible oscillations of L_z on the SMBH orbital timescale. As is visible, these oscillations are important for most of the plunges and EMRIs. There is also a visible preference for driving stars with positive L_z to become EMRIs or plunges, which is discussed briefly in the text.

in our simulations is best demonstrated in Fig. 6. This is Fig. 4 with a non-normalized azimuthal angular momentum. In this plot the importance of region where $L_{\text{plunge}} + \Delta L_b$ is clear and it approximately bounds most EMRIs and plunges. This is because stars with $L_z < L_{\text{plunge}} + \Delta L_b$ region are those that can reach L_{plunge} via the Kozai effect, and therefore plunge into the primary SMBH or become EMRIs.

Interestingly, there is also a clear asymmetry about $L_z = 0$. This is a result of the a symmetry broken by the handedness of the secondary SMBH. When the orbit of the star is in the same sense as that of the secondary SMBH the star is more likely to reach higher

eccentricities and ultimately become a plunge or EMRI. This is likely due to increasing the apparent period of the secondary SMBH during prograde GR precession. This increases the duration over which the torques from the binary are exerted and ultimately the total magnitude of ΔL_b .

6.7 Changes in angular momentum on the orbital timescale of the star

Between periastris passages a star will undergo a change in angular momentum which is typically of size

$$\Delta L_* \sim \frac{dL}{dt} P_* \sim \frac{qGMa_*^2}{a_*^3} P_* = \frac{GMq}{a_*} \left(\frac{a_*}{a_\bullet}\right)^3 P_*, \quad (49)$$

which gives

$$\frac{\Delta L_*}{L_c} = 2\pi q \left(\frac{a_*}{a_\bullet}\right)^3 = 2\pi q \left(\frac{P_*}{P_\bullet}\right)^2. \quad (50)$$

This is naturally of order P_*/P_\bullet , smaller than the oscillations on the SMBH binary timescale given by Eqn. 45. The importance in these oscillations is that while they remain small the star approaches L_{plunge} more smoothly i.e. the discrete periastris passages are closely spaced in angular momentum and periastris distance. This is elucidated in the following subsection.

6.8 Parameter Space

To understand the effects of the various mechanisms discussed in this section, we plot the limits that they define in Fig. 7. The initial angular momentum, normalized by L_c , is plotted against the initial semi-major axis of the stars in our simulation with $q = 0.3$ and $m_* = 10M_\odot$. In the upper panel we plot the initial *total* angular momentum of the stars, while in the lower panel we plot the initial *z* component of the angular momentum. Stars that result in EMRIs are demarcated by gold stars, stars that plunge by green dots, stars that become unbound by orange dots, and all other stars by blue dots.

The secondary stalls at the stalling radius labeled R_{Stall} . At this point the primary has a resultant Hill radius labeled R_{Hill} . We define the Hill radius around the primary as the radius inside of which the Jacobi constant cannot be small enough to cross the L_2 Lagrange point beyond the secondary and exit the system (Murray & Dermott 2000). The stars that are unbound and ejected from the system are orange and restricted to semi-major axes greater than the Hill radius.

Lines are shown where the timescales estimated above are equal: $t_{\text{Kozai}} = t_{\phi, \text{SP}}$ (dotted black), $t_{\text{Kozai}} = t_{\phi, \text{GR}}$ (solid black diagonal), $P_\bullet = t_{\phi, \text{GR}}$ (long dashed black). Also plotted are lines demonstrating the size of changes in angular momentum during the binary's orbit ΔL_b (short dashed black), and over an orbit of the stars ΔL_* (dash dot black). For orbits close with L close to L_{plunge} then the far field approximation of Eqn. 39 is inaccurate. This is the reason for the curvature of the $t_{\text{Kozai}} = t_{\phi, \text{GR}}$ line, which is calculated using the geodesic equation.

Near or outside the Hill radius stars evolve by strong interactions with the secondary SMBH and the Kozai effect is not relevant. As is visible from the figure it is less probable that these ‘‘chaotic orbits’’ turn into plunges or EMRIs than stars farther in which are affected by the Kozai mechanism.

Well within the Hill radius the Kozai mechanism is most accurate. By the standard Kozai formalism no star with an initial L_z

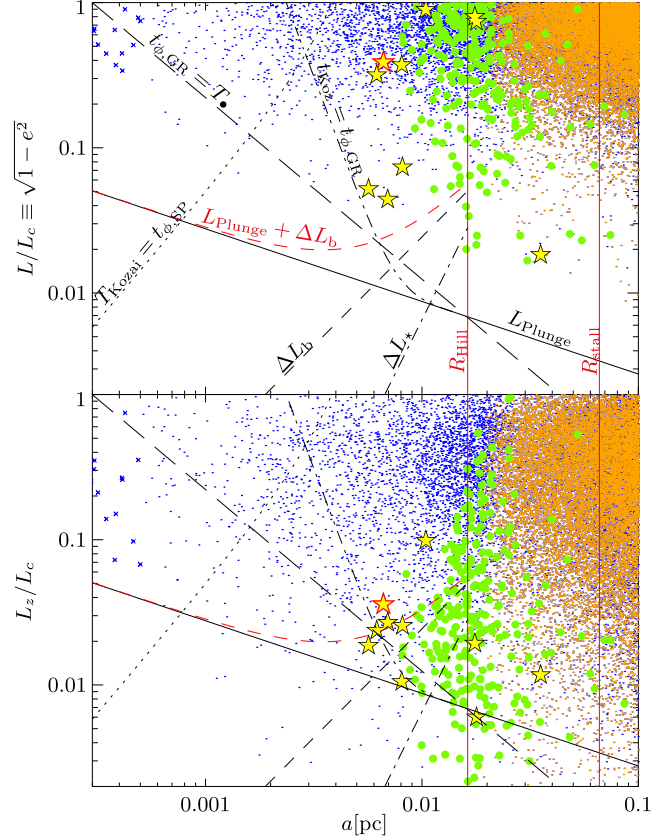


Figure 7. A parameter space plot showing outcomes as function of normalised angular momentum and semi-major axis along with important delimiting lines as discussed in Sec. 6. Initial L/L_c and L_z/L_c are plotted in the upper and lower panels respectively. Each star is represented by its outcome: an EMRI (gold star), a plunge (green dot), becoming unbound (orange dot), reaching our computational limit of 10^{10} steps (blue cross), or remaining in the cusp at the conclusion of our simulation (blue dot). The particular simulation shown is $q = 0.3$ and $m_* = 10M_\odot$.

much greater than L_{plunge} should plunge (or form an EMRI), since L_z is conserved. However, due to oscillations in L , (ΔL_b) which occur on the binary orbital timescale and are not accounted for in the Kozai formalism stars with higher L_z can still become plunges or EMRIs if $L_z \lesssim L_{\text{plunge}} + \Delta L_b$.

The plunges and EMRIs lie to the right of the Schwarzschild barrier ($t_{\text{Kozai}} = t_{\phi, \text{GR}}$) since to the left of this line GR precession dominates the evolution and it is not possible to reach low angular momenta before the orbit precesses and the tidal torque is reversed.

Moreover, in the region with a small but to the right of $t_{\text{Kozai}} = t_{\phi, \text{GR}}$, the changes of angular momentum over each orbit (ΔL_*) are small and therefore stars gradually approach L_{plunge} . As a result these stars undergo close periastris passages and lose their energy to gravitational radiation instead of directly plunging. To the right of this region, with larger a , the change in angular momentum on each orbit becomes larger, and stars are more likely to plunge directly into the primary than become EMRIs.

6.9 Synopsis

There are essentially three different ways of producing EMRIs in the context of widely-separated binary SMBHs: 1) single or multiple strong interactions with the secondary SMBH which cause the compact object to fortuitously pass close to the primary; 2) Kozai oscillations mixed with oscillations on the timescale of the secondary which drive the star to high eccentricity and has some significant probability of plunging but instead has a close passage; and 3) stars which are also driven to high eccentricity from Kozai oscillations mixed with oscillations on the timescale of the secondary, but approach the Schwarzschild barrier before, but in the near vicinity of L_{plunge} . In our simulations the first of these methods is sub-dominant, and so we focus on the latter two.

In both cases the initial process is the same and so we shall describe them together. The star must begin with a low L_z such that $L_z \leq L_{\text{plunge}} + \Delta L_b$. This alone is necessary but not sufficient to ensure that a star will reach L_{plunge} . Secondly, the star should have a semi-major axis which is at most a factor of a few smaller than R_{Stall} . This avoids the strong scatterings by the secondary that are most likely to eject the star from the system, and instead results in Kozai-Lidov oscillations. However, the semi-major axis of the star can not be so low that the Kozai period becomes too long and GR precession dominates the evolution ($t_{\text{Kozai}} > t_{\phi, \text{GR}}$) before reaching low angular momenta. In this case the orbit will precess and the tidal torque that drives the Kozai-Lidov oscillations will be reversed well before L_{plunge} . GW radiation therefore cannot act efficiently to drive the star to be an EMRI.

In our simulations we find a ‘sweet spot’ where the semi-major axis is just larger than the Schwarzschild barrier. In this region the changes in angular momentum between periapsis passages are small ($\Delta L_* \ll L_{\text{plunge}}$). The star therefore has close periapsis passages in which it can radiate orbital energy in GWs, forming an EMRI before plunging beyond the Schwarzschild radius. At larger semi-major axes the change in periapsis distance per orbit is larger, and stars are more likely to plunge directly into the primary SMBH.

7 DISCUSSION

7.1 EMRI Rates

Under the previous design of LISA EMRIs consisting of a $10^6 M_\odot + 10 M_\odot$ black hole system would be detectable to a redshift of $z \sim 1$ (dimensionless spin $a/M = 0.9$, averaged over orientations, Amaro-Seoane et al. 2007) giving a co-moving detection volume of 160 Gpc^3 . The rate of EMRIs from SMBH binaries estimated here of $\mathcal{R}_{\text{EMRI}} = 8 \times 10^{-4} \text{ yr}^{-1} \text{ Gpc}^{-3}$ (table 5), gives a detection rate of $\sim 0.12 \text{ yr}^{-1}$, and therefore ~ 0.6 over a five year mission.

This is particularly interesting since EMRI waveforms contain information about the presence of both gas (Narayan 2000; Yunes et al. 2011) and the secondary SMBH (Yunes, Miller & Thornburg 2011). The importance of gas is significant, since due to the same mechanisms discussed here, a large number of tidal disruptions are also expected (Chen, Liu & Magorrian 2008; Wegg & Bode 2011; Chen et al. 2011). Thus, any EMRI observed with the signal of a secondary SMBH in its waveform formed by the mechanisms discussed here are likely to be in the presence of gas.

It is important to note that our rates are proportional to the number density of compact objects at about $R_{\text{Stall}}/10 \sim 0.01 \text{ pc}$. Note that this is in contrast to the standard picture of isolated SMBH EMRI formation where the rate scales with the product

of the number density of compact objects and that of stars (e.g. Hopman 2009). Therefore, in the fully mass segregated case, the isolated SMBH EMRI formation rate scales with the square of the number density of compact objects. We discuss some of our assumptions which affect the number density of compact objects in Sec. 7.2.

There is another key consequence of the EMRI formation mechanism presented here, which is outside the scope of this work: In the standard picture of EMRI formation stars must scatter to a state with low overall L , while in the Kozai picture stars need only a low L_z (i.e. the standard loss cone is instead the entire Kozai wedge, see Figs. 4 and 6). Thus, for the duration of the secondary’s time at the stalling radius, interactions (such as star-star scattering, or non-conservation of L_z due to the octopole term Lithwick & Naoz 2011) need only drive stars to low L_z (or more accurately low $L_z + \Delta L_b$, see Sec. 6.8) for them to be able to form EMRIs under the Kozai mechanism. This situation is similar to the predicted increased rates of tidal disruption in axisymmetric nuclei. In this case the rates are increased by a factor of a few from spherical nuclei (Magorrian & Tremaine 1999; Vasiliev & Merritt 2013). We therefore conservatively expect an increase of at least this factor in the EMRI rate while the secondary SMBH is stalled. However there is at least one reason to suspect rate increase would be higher than this: The oscillations on the timescale of the SMBH binary (Sec. 6.6) do not occur in axisymmetric nuclei, and these expand the size of the loss cone. The situation warrants further investigation but is beyond the scope of this work.

7.2 Assumptions

Schwarzschild Black Holes: Throughout this work, in common with the vast majority of studies on the formation of EMRIs, we neglect the spin of the SMBH. This is a short coming that is only beginning to be overcome (Amaro-Seoane, Sopuerta & Freitag 2013). We make this choice for simplicity, since there is increasing observational evidence that at least some SMBHs have significant spin (Brenneman & Reynolds 2006). Apart from very close passages, even in the presence of spin, the precession will be dominated by the Schwarzschild terms (Merritt, Schnittman & Komossa 2009). Instead the largest effect on this work would be Lense-Thirring precession of the star’s orbital plane since, if the BH spin is not aligned with the orbital plane, this would result in non-conservation of L_z . We speculate this could therefore increase the rate of EMRIs and plunges since more stars can potentially undergo Kozai oscillations which result in close BH encounters. To lowest order in v/c the angular momentum of a test particle in the Kerr metric precesses due to Lense-Thirring precession at a rate (Merritt 2013, we neglect the quadrupolar term in this order of magnitude estimate)

$$\frac{d\mathbf{L}}{dt} = \frac{4\pi}{P_*} \left(\frac{GM}{Lc} \right)^3 (\boldsymbol{\chi} \times \mathbf{L}) \quad (51)$$

where $\boldsymbol{\chi}$ is the dimensionless spin vector of the black hole. Over n orbits we therefore expect a change in L_z of

$$\Delta L_z \approx 4\pi n \left(\frac{GM}{Lc} \right)^3 (\boldsymbol{\chi} \times \mathbf{L})_z \quad (52)$$

The majority of the EMRIs have initial semi-major axis $a \approx 0.007 \text{ pc}$ and have $n \approx 20,000$ orbits over the entire length of our simulations. For a favourably oriented spinning hole then, over our simulation, stars at this semi-major axis change their L_z by

$$\frac{\Delta L_z}{GM/c} \approx \frac{1.7\chi}{1 - e^2}. \quad (53)$$

Therefore even over the ≈ 1 Myr length of our simulations a significant fraction of stars at this radius could have their L_z secularly changed by of order the size of the loss cone by a spinning black hole. These perturbations would continue for the entire length of time that the binary is stalled.

Cusp Profile: One of the major factors in determining the rates is the stellar distribution. In our simulations we use an η -model (Tremaine et al. 1994) of a spherical stellar cusp with a central SMBH to establish the stellar distribution (see Sec. 3.3). This is a self-consistent family of models of a stable isotropic stellar cusp. In our simulations, we have chosen $\eta = 1.75$, the value appropriate for a relaxed stellar cusp. However, there is a complication: the galaxy where we can best resolve the inner parsec is our own Milky Way, and as yet there is no consensus on the existence of a cusp (Buchholz, Schödel & Eckart 2009; Bartko et al. 2010; Do et al. 2009; Yusef-Zadeh, Bushouse & Wardle 2012). An alternative interpretation to a lack of a steep visible cusp is that a density cusp is present in the Galactic center, but is ‘dark’ as a result of mass segregation causing the density to be dominated by COs (Freitag, Amaro-Seoane & Kalogera 2006; Preto & Amaro-Seoane 2010). Our rates scale roughly linearly with the number density of stellar mass black holes at $R_{\text{stall}}/10 \sim 0.01$ pc, allowing them to easily be rescaled to other cusp profiles (and other CO number densities).

Stellar Interactions: We have not considered relaxation processes such as those due to star-star scattering or star-bulk scattering.

The timescale for relaxation via star-star scattering is approximately 1 Gyr at r_c (Amaro-Seoane & Preto 2011), much longer than the duration of our simulations, and is not a strong function of r in the cusp (Alexander 2005). However, care must be taken: This approximation is not as accurate as might be assumed because the timescale to change angular momentum by of order itself will be reduced for high eccentricity orbits by a factor $\sim (1-e^2)$ (Hopman & Alexander 2005). Therefore, for the highest eccentricity stars in our simulation relaxation could be beginning to become non-negligible.

In the case of star-bulk relaxation such as that due to resonant relaxation or asymmetric bulges the timescales can be much shorter. For instance, consider resonant relaxation. In this case the comparable timescale to t_{Kozai} is given by (Merritt et al. 2011b)

$$t_{\text{rr}} = \sqrt{N_*(< a_*)} \frac{M}{M_*(< a_*)} \frac{P_*}{2\pi} \sqrt{1-e^2}. \quad (54)$$

Here $N_*(< a_*)$ is the number of stars inside the semi-major axis of the test star. Equating t_{rr} to t_{Kozai} we can solve for the semi-major axis where the two effects are comparable:

$$a_{\text{rr}} = 0.004 \left(\frac{R_{\text{stall}}}{0.07 \text{ pc}} \right)^{24/19} \left(\frac{q}{0.3} \right)^{-8/19} \left(\frac{M/m_*}{10^5} \right)^{-4/19} \text{ pc}. \quad (55)$$

Inside of a_{rr} resonant relaxation would be the dominant form of precession while further out the Kozai torques would dominate the evolution. While a_{rr} is about a factor of 2 smaller than where our innermost EMRIs are sourced it could have an impact on our results. However, this is beyond the scope of this work.

SMBH merger rate: While in recent years there has been significant progress in understanding the merger rates of SMBHs, there still remains a great deal of uncertainty. Indeed, this is one of the unknowns that LISA or a LISA-like experiment would estimate. Here we have made the crude approximation that every $10^6 M_\odot$ SMBH will undergo one major merger per Hubble time with a constant probability over time. While it is certain that neither of these assumptions is quite right, we expect the uncertainties here to be minimal when compared to those relating to the stel-

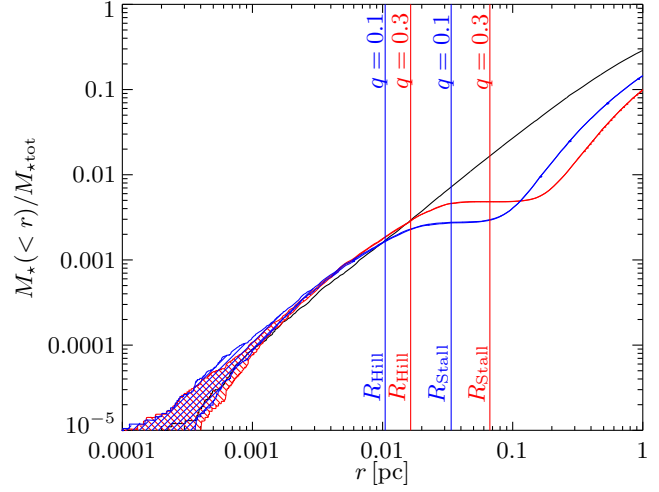


Figure 8. We plot the stellar mass interior to a given radius normalized to the total stellar mass, $M_*(< r) / M_{*tot}$. In black we plot the initial cumulative stellar mass (c.f. Eqn. 5), while in blue we plot the cumulative stellar mass at the end of the simulation for the $q = 0.1$, $m_* = 10 M_\odot$ run, and in red we plot the cumulative stellar mass at the end of the simulation for the $q = 0.3$, $m_* = 10 M_\odot$ run. Note that the initial conditions for all runs are the same. The only difference between the outcomes of the runs with the same q but different stellar masses is due to those stars which go within $100 GM/c^2$, only a small fraction of all stars. Thus, the cumulative stellar mass for the runs with $m_* = 1 M_\odot$ are virtually the same as the $10 M_\odot$ counterparts with the same q . The hatched regions are stars that had not completed the full simulation within the preset limit of 10^{10} steps. For reference we also plot the stalling radii of the secondary as vertical lines.

lar cusp, or, potentially, the lack thereof. For this reason we have chosen simplicity over false precision.

Invariant stellar potential: One inconsistency of our methodology is the assumption that the stellar potential does not evolve with time, though the stars’ orbits do. To demonstrate the possible effect of such an assumption we plot the mass interior to a given radius as a function of radius in Fig. 8. There the solid black line is the initial distribution given by Eqn. 5, the red solid line is the curve for the $q = 0.3$ and $m_* = 10 M_\odot$ simulation, and the blue solid curve is for the $q = 0.1$ and $m_* = 10 M_\odot$ simulation. The mass of the star has little effect on these curves. The filled region represents stars that required more than 10^{10} steps to complete the simulation and were therefore terminated. From Figs. 4 and 6 most EMRIs originate from $\approx 10^{-2}$ pc and at this position the mass interior has not changed significantly. Thus, this assumption would not likely have a significant impact on our findings.

8 CONCLUSION

We have considered the possibility of extreme mass-ratio inspirals (EMRIs) that form as a result of a secondary supermassive black hole (SMBH) inspiraling towards a primary SMBH. Using a symplectic integrator to follow the paths of 10^6 non-interacting stars around a primary $10^6 M_\odot$ SMBH with various values for both the stellar mass and an inspiraling secondary SMBH, we have reached several conclusions:

- (i) EMRIs can be formed by binary SMBH systems with numbers which could be detectable by future space-based gravitational wave missions.
- (ii) Frequently overlooked, oscillations on the timescale of the

secondary SMBH, and which deviate from the traditional Kozai-Lidov mechanism, are fundamental to the formation of almost all EMRIs and plunges.

- (iii) The region of parameter space where precession due to GR, $t_{\phi,GR}$, and the precession due to the Kozai-Lidov mechanism, t_{Kozai} , are comparable (the Schwarzschild barrier: $t_{\phi,GR} = t_{Kozai}$) causes important dynamical effects.
- (iv) When a star has a semi-major axis such that $t_{Kozai} < t_{\phi,GR}$, neither EMRIs nor plunges are possible since the precession rate due to GR will increase before the angular momentum of the star falls sufficiently to plunge or become an EMRI.
- (v) When a star has a semi-major axis such that $t_{Kozai} > t_{\phi,GR}$, EMRIs are formed most often when the star has a smaller semi-major axis, since it will gradually approach the plunge angular momentum (small ΔL_*). At higher semi-major axes plunges are more likely.

It is also interesting that the formation of EMRIs by the channel described here is verifiable: While we have shown that it is possible for EMRIs to be formed in SMBH binaries, it has also been shown that, if such an EMRI were to form and be detected, it is possible that the waveform provides information about the mass of the secondary SMBH and the binary separation (Yunes, Miller & Thornburg 2011). This is of particular interest since, by inferring the existence of a SMBH binary at wide separation, it would extend the range of SMBH binary separations to which low frequency gravitational wave detectors are sensitive.

9 ACKNOWLEDGMENTS

We gratefully acknowledge a significant amount of guidance from Sterl Phinney, many insights regarding resonant relaxation from David Merritt, and useful conversations with Sotiris Chatzopoulos, Chris Hirata, Smadar Naoz and Michele Vallisneri.

Support for this work was provided by NASA BEFS grant NNX-07AH06G.

REFERENCES

- Alexander T., 2005, *Physics Reports*, 419, 65
 Alexander T., Hopman C., 2009, *ApJ*, 697, 1861
 Aller M. C., Richstone D., 2002, *AJ*, 124, 3035
 Amaro-Seoane P. et al., 2012, arXiv, astro-ph, 1201.3621
 Amaro-Seoane P., Gair J. R., Freitag M., Miller M. C., Mandel I., Cutler C. J., Babak S., 2007, *Classical and Quantum Gravity*, 24, 113
 Amaro-Seoane P., Preto M., 2011, *Classical and Quantum Gravity*, 28, 094017
 Amaro-Seoane P., Sopuerta C. F., Freitag M. D., 2013, *MNRAS*, 429, 3155
 Antognini J. M., Shappee B. J., Thompson T. A., Amaro-Seoane P., 2013, arXiv, astro-ph, 1308.5682
 Bahcall J. N., Wolf R. A., 1976, *ApJ*, 209, 214
 Barack L., Cutler C., 2004, *Phys. Rev. D*, 69, 82005
 Bartko H. et al., 2010, *ApJ*, 708, 834
 Begelman M. C., Blandford R. D., Rees M. J., 1980, *Nature*, 287, 307
 Binney J., Tremaine S., 2008, *Galactic Dynamics: Second Edition*, Binney, J. & Tremaine, S., ed. Princeton University Press
 Blaes O., Lee M. H., Socrates A., 2002, *ApJ*, 578, 775
 Brenneman L. W., Reynolds C. S., 2006, *ApJ*, 652, 1028
 Buchholz R. M., Schödel R., Eckart A., 2009, *A&A*, 499, 483
 Chen X., Liu F. K., Magorrian J., 2008, *ApJ*, 676, 54
 Chen X., Madau P., Sesana A., Liu F. K., 2009, *ApJL*, 697, L149
 Chen X., Sesana A., Madau P., Liu F. K., 2011, *ApJ*, 729, 13
 Côté P. et al., 2004, *ApJS*, 153, 223
 Do T., Ghez A. M., Morris M. R., Lu J. R., Matthews K., Yelda S., Larkin J., 2009, *ApJ*, 703, 1323
 Freitag M., Amaro-Seoane P., Kalogera V., 2006, *ApJ*, 649, 91
 Gair J. R., Barack L., Creighton T., Cutler C., Larson S. L., Phinney E. S., Vallisneri M., 2004, *Classical and Quantum Gravity*, 21, 1595
 Gair J. R., Kennefick D. J., Larson S. L., 2005, *Phys. Rev. D*, 72, 84009
 —, 2006, *ApJ*, 639, 999
 Ghez A. M. et al., 2008, *ApJ*, 689, 1044
 Grossman R., Levin J., 2009, *Phys. Rev. D*, 79, 043017
 Hils D., Bender P. L., 1995, *ApJL*, 445, L7
 Holman M., Touma J., Tremaine S., 1997, *Nature*, 386, 254
 Hopman C., 2009, *Classical and Quantum Gravity*, 26, 094028
 Hopman C., Alexander T., 2005, *ApJ*, 629, 362
 —, 2006, *ApJL*, 645, L133
 Hughes S. A., 2009, *ARA&A*, 47, 107
 Ivanov P. B., Polnarev A. G., Saha P., 2005, *MNRAS*, 358, 1361
 Katz B., Dong S., 2012, ArXiv e-prints
 Katz B., Dong S., Malhotra R., 2011, *Physical Review Letters*, 107, 181101
 Kozai Y., 1962, *AJ*, 67, 591
 Levin Y., 2003, arXiv, astro-ph, 0307084
 Levin Y., Beloborodov A. M., 2003, *ApJ*, 590, L33
 Lidov M. L., 1962, *Planet. Space Sci.*, 9, 719
 Lithwick Y., Naoz S., 2011, *ApJ*, 742, 94
 Magorrian J., Tremaine S., 1999, *MNRAS*, 309, 447
 Menou K., Haiman Z., Kocsis B., 2008, *New A Rev.*, 51, 884
 Merritt D., 2013, *Dynamics and Evolution of Galactic Nuclei*
 Merritt D., Alexander T., Mikkola S., Will C., 2011a, *Phys. Rev. D*, 84, 44024
 —, 2011b, *Phys. Rev. D*, 81, 62002
 Merritt D., Schnittman J. D., Komossa S., 2009, *ApJ*, 699, 1690
 Miller M. C., Freitag M., Hamilton D. P., Lauburg V. M., 2005, *ApJ*, 631, L117
 Milosavljević M., Merritt D., 2003, *ApJ*, 596, 860
 Murray C. D., Dermott S. F., 2000, *Solar System Dynamics*
 Narayan R., 2000, *ApJ*, 536, 663
 O’Leary R. M., Kocsis B., Loeb A., 2009, *MNRAS*, 395, 2127
 Paczyński B., Wiita P., 1980, *A&A*, 88, 23
 Peter A. H. G., 2008, PhD thesis, Princeton University (Publication No. AAT 3305294.)
 —, 2009, *Phys. Rev. D*, 79, 103531
 Peters P. C., 1964, *Phys. Rev. D*, 136, 1224
 Preto M., Amaro-Seoane P., 2010, *ApJL*, 708, L42
 Preto M., Tremaine S., 1999, *AJ*, 118, 2532
 Ryan F. D., 1997, *Phys. Rev. D*, 56, 1845
 Sesana A., Haardt F., Madau P., 2008, *ApJ*, 686, 432
 Sesana A., Vecchio A., Eracleous M., Sigurdsson S., 2008, *MNRAS*, 391, 718
 Thompson T. A., 2011, *ApJ*, 741, 82
 Tremaine S., Richstone D. O., Byun Y.-I., Dressler A., Faber S. M., Grillmair C., Kormendy J., Lauer T. R., 1994, *AJ*, 107, 634
 Vasiliev E., Merritt D., 2013, *ApJ*, 774, 87
 Wegg C., 2012, *ApJ*, 749, 183
 —, 2013, PhD thesis, California Institute of Technology

Wegg C., Bode J. N., 2011, *ApJL*, 738, L8

Yunes N., Kocsis B., Loeb A., Haiman Z., 2011, *Physical Review Letters*, 107, 171103

Yunes N., Miller M. C., Thornburg J., 2011, *Phys. Rev. D*, 83, 44030

Yusef-Zadeh F., Bushouse H., Wardle M., 2012, *ApJ*, 744, 24